Available online at www.sciencedirect.com

ScienceDirect

Geochimica et Cosmochimica Acta 268 (2020) 383–404

Geochimica et Cosmochimica Acta

www.elsevier.com/locate/gca

Importance of the size and distribution of chemical heterogeneities in the mantle source to the variations of isotope ratios and trace element abundances in mid-ocean ridge basalts

Boda Liu *, Yan Liang

Department of Earth, Environmental and Planetary Sciences, Brown University, Providence, RI 02912, United States

Received 19 December 2018; accepted in revised form 7 October 2019; available online 15 October 2019

Abstract

The size and distribution of chemical heterogeneities in the mantle source affect compositions of basalts erupted on the surface. To understand the effect of size and distribution of heterogeneous mantle source on the variations of isotope ratios and incompatible trace element abundances in mid-ocean ridge basalts (MORB), we develop a time-dependent two-porosity ridge model that features disequilibrium melting and channelized melt migration in a truncated triangular melting region. We run numerical simulations for a two-component mantle that consists of the depleted mantle and enriched blobs spanning a range of enriched compositions and sizes. The volume fraction of enriched mantle varies under 10% of the mantle source and the size of the melt production area that contributes to the pooled melt is also treated as a variable. Results show that higher abundance of incompatible trace element in the enriched mantle, larger size of enriched blobs, and narrower melt pooling area produce larger variations of isotope ratios in the pooled melt. We develop an empirical scaling equation that quantifies the fluctuation of isotope ratios as a function of elemental abundance, size and average spacing of enriched heterogeneities in the source, and the width of melt pooling area. The two-standard deviation of $^{143}Nd/^{144}Nd$, $^{176}Hf/^{177}Hf$, $^{87}Sr/^{86}Sr$, and $^{206}Pb/^{204}Pb$ in global MORB not affected by hotspots can be produced by melting a two-component mantle with 5.2–8.2% enriched heterogeneities of 5.1–6.7 km mean size and 7.0(±1.6), 5.3(±1.2), 2.0(±0.5), and 9.8(±2.2) times higher abundances of Nd, Hf, Sr, and Pb than the depleted mantle, respectively. Incomplete mixing of melts at the base of the lithosphere is likely important for producing the variation of incompatible trace elements in MORB. The melt erupted at the ridge axis may represent an ensemble of the melt pooled from the center of the melt pooling area and melts pooled from local areas away from the ridge axis. The present study underscores the importance of the size and distribution of mantle heterogeneities to the interpretation of isotope ratios and trace element abundances in basalts.

Keywords: Mantle heterogeneity; Size of mantle heterogeneity; Distribution of mantle heterogeneity; Isotope ratios; Trace elements; Mid-ocean ridge basalts; Off-axis seamount; Magma mixing; Melt migration; Two-porosity model; Disequilibrium melting; 2D time-dependent model

1. INTRODUCTION

The source regions of mid-ocean ridge basalts (MORB) are heterogeneous, consisting of chemically and lithologically distinct domains of variable size and distribution.

* Corresponding author.
E-mail addresses: boda_liu@hotmail.com (B. Liu), yan_liang@brown.edu (Y. Liang).

https://doi.org/10.1016/j.gca.2019.10.013
0016-7037/

Partial melting of such heterogeneous mantle sources gives rise to diverse isotopic compositions of basalts and residual peridotites (e.g. Zindler and Hart, 1986; Hofmann, 2003; Stracke, 2012). Variations of isotope ratios of basalts are generally interpreted on the basis of mixing in the geochemical literature. However, it is difficult to ascertain whether mixing takes place before, after or during melting and melt migration in the melting region. For example, the inverse correlation between $^{87}Sr/^{86}Sr$ and $^{143}Nd/^{144}Nd$ in oceanic basalts can be accounted for by either mixing of depleted and enriched mantle reservoirs or mixing of melts derived from the depleted and enriched mantle sources. To further interpret geochemical mixing calculations, one must consider melting and melt migration processes.

For melting in an upwelling mantle, the size and spatial distribution of heterogeneous mantle sources feeding into the melting region are important for the interpretation of isotope ratios and trace element abundances in eruptible melts. Two recent studies (Liu and Liang, 2017a; Liang and Liu, 2018) showed that the shape of a chemical heterogeneity marked by isotope ratios in the mantle rock would be deformed by melting and melt migration. The chemical heterogeneity would stretch as the transport velocity of the relevant incompatible element increases (Liang and Liu, 2018). The chemical heterogeneity would also be smeared when there is local chemical disequilibrium between the percolating melt and the residual solid (Liu and Liang, 2017a). The isotopic signal of the enriched mantle is progressively diluted while that of the surrounding depleted mantle becomes more enriched. Stretching and smearing alter the composition of the residue directly and change the composition of melts that are collected and mixed to form on-axis MORB. Therefore, quantifying the effect of stretching and smearing of chemical heterogeneities is necessary for any geochemical model trying to link MORB and residue samples to the mantle source.

The melt migration induced mixing is important only when the composition of mantle source is heterogeneous and the size of enriched mantle is considered. In this study, we systematically examine the effects of composition, size and spatial distribution of chemical heterogeneities in the mantle source on the variations of isotope ratios of Nd, Hf, Sr, and Pb and selected incompatible trace elements in the erupted melts. We develop a pseudo-2D two-porosity ridge model for disequilibrium melting, melt transport, and melt pooling in an upwelling chemically heterogeneous mantle (Section 2). We set the size, spatial distribution, and composition of chemical heterogeneities in the mantle source and use time-dependent numerical simulations to study how the enriched isotopic signals are transported through the melting region and mixed in the decompaction boundary layer (Section 3). We show that isotopic variability in the pooled melt depends on the size of the melt pooling area. We derive a scaling relationship that can be used to predict isotopic variability in the pooled melt (Section 4). We argue that incomplete mixing in the lateral direction is needed to account for the ranges of variations in Sr, Pb, Nd, and Hf isotope ratios and incompatible trace element abundances in global MORB not affected by hotspots. The present study demonstrates the importance of the size and distribution of mantle heterogeneities, the size of melt pooling area, mantle composition, and melt generation processes to the interpretation of chemical variations observed in MORB.

2. THE PSEUDO-2D RIDGE MODEL

2.1. Model domain and set-up of enriched blobs

To model trace element and isotope compositions of primitive MORB, one has to consider the geometry of the melting region (O'Hara, 1985). The standard geochemical treatment of this problem is the melting triangle (e.g. Holness and Richter, 1989; Plank et al., 1995). In this class of ridge models, the mantle source is homogeneous and the problem is time-independent. For heterogeneous mantle source, previous models consider mixing of melts derived from depleted and enriched components in the mantle reservoir or melting of a well-mixed mantle that consists of depleted and enriched components (e.g. Morgan and Morgan, 1999; Ito and Mahoney, 2005a,b; Stracke and Bourdon, 2009; Rudge et al., 2013; Wanless et al., 2014). In this class of melting models, the enriched and depleted components in the mantle source are spatially homogeneous and the problem is time-independent. In a more general setting, the enriched and depleted mantle components may distribute spatially in the mantle source and their size needs to be considered in the melting model. The melting problem is time-dependent (e.g. DePaolo, 1996; Liang, 2008; Weatherley and Katz, 2016; Keller et al., 2017; Liang and Liu, 2018; Bo et al., 2018).

Fig. 1 is a schematic diagram showing our model setup where enriched blobs of various sizes enter the base of the melting region from below. We consider melting a two-component mantle that consists of randomly distributed enriched chemical heterogeneities in the depleted background mantle (Fig. 1b). We assume that the enriched chemical heterogeneity and depleted mantle have the same mineralogy and major element composition and thus the same melting behavior. The size, shape, and distribution of the enriched heterogeneities in the mantle are unknown. As a starting model, we consider an endmember case in which the shape of enriched mantle blobs feeding into the melting region from below is circular and their spatial distribution is random. Such a heterogeneous mantle source can be described mathematically as a time-dependent boundary condition at the bottom of the melting region by superposition of individual heterogeneities in the 2D domain. For a series of Gaussian-shape heterogeneities, the mantle composition feeding into the melting column is given by the expression:

$$C_s^0(x,t) = C_D + \sum_{i=1}^{n} \left(C_E^i - C_D\right) \cdot \exp\left(-\left(\frac{V_0 \cdot (t - t_i)}{\sigma_i}\right)^2 - \left(\frac{x - x_i}{\sigma_i}\right)^2\right), \quad (1)$$

where C_s^0 is the concentration of the trace element in the mantle source; C_D and C_E^i are concentrations of the depleted mantle and the endmember concentration in the

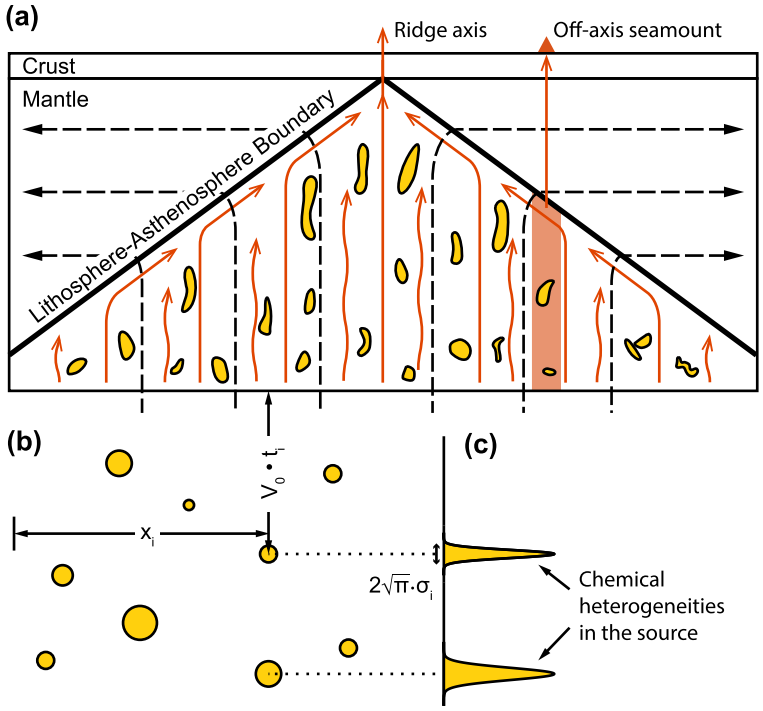

Fig. 1. Schematic diagram showing the pseudo-2D ridge model for melting in an upwelling chemically heterogeneous mantle. Orange blobs in panel (a) represent chemical heterogeneities. Dashed lines indicate mantle flow direction. Red lines without waves illustrate melt flows in the high-porosity channel while wavy red lines illustrate melt flows in the porous matrix. Thick lines are lithosphere-asthenosphere boundaries (LABs). Under the LAB, melts are passively focused to the axis to form the pooled melt. A local melt pooling area is shown as a color-shaded bin. Panel (b) shows an idealized case of randomly distributed circle-shaped heterogeneities in the background of depleted mantle. The position of individual heterogeneity in the source can be determined by the horizontal position, x_i, and the distance below the bottom of the melting region. The latter is the product of the upwelling rate of the mantle, V_0, and the time that the heterogeneity enters the melting region, t_i. Panel (c) shows a vertical concentration profile in the source mantle. Enriched heterogeneities are Gaussian-shaped and their sizes are defiend as $L = 2\sqrt{\pi}\cdot\sigma_i$. (For interpretation of the references to colour in this figure legend, the reader is referred to the web version of this article.)

i-th enriched heterogeneity; t_i is the time when the i-th heterogeneity enters the melting region; x_i is the horizontal position of the i-th heterogeneity; σ_i is a parameter in the Gaussian function. Key symbols are listed in Table 1.
The size of the heterogeneity is defined as:

$$L_i = 2\sqrt{\pi}\cdot\sigma_i. \quad (2)$$

We treat the 2D melting region as two overlapping continua consisting of low-porosity residual lherzolite and harzburgite (referred to as the matrix continuum or matrix hereafter) and high-porosity interconnected dunite channels (or channel continuum). Part of the melt generated in the matrix is extracted into the channel while the remaining interstitial melt percolates through and exchanges chemically with the porous residue matrix. For convenience, we refer interstitial melts in the matrix and channel continua as the "matrix melt" and the "channel melt", respectively.

The model domain is a 60 km × 100 km triangular melting region. We assume the same dry solidus for the enriched and depleted mantle reservoirs and melt produced in regions beyond the 100 km-width of the domain completely solidifies at the base of the lithosphere (Asimow et al., 2004). The size of the melting region and the degree of melting should sustain a melt flux capable of producing a 6 km thick oceanic crust. For a constant and uniform melting rate, this can be achieved by setting the maximum degree of melting at the ridge axis to 20%. The triangular melting region consists of a bundle of two-porosity melting columns that consist of the matrix and channel continua (Yao et al., 2010). To focus on chemical variations, we assume that porosity, melt and solid velocities in the matrix and channel continua in each melting column are independent of time and horizontal coordinate. (The effect of horizontal melt flow is discussed in Section 5.) Hence our bundle of column model is a pseudo-2D model in which lateral melt and solid flows in the melting region are neglected.

Matrix and channel melts emerging at the top of each melting column percolate toward the ridge axis along a sloping decompaction channel at the lithosphere-asthenosphere boundary or LAB (Sparks and Parmentier, 1991; Spiegelman, 1993; Hebert and Montési, 2010). Melt migration along the thin decompaction channel can be time-dependent due to presence of porosity waves (e.g. Spiegelman, 1993; Ghods and Arkani-Hamed, 2000). This complicated process will not be treated in the present study. Instead, we consider two endmember cases: complete mix-

Table 1
Key symbols.

Symbols	Meaning	Values
C_s^0	Concentration of trace element in the mantle source	
C_s^m, C_f^m, C_f^{ch}	Concentration of trace element in the residue, matrix melt, or channel melt	
d	Average grain size	
Da	Damköhler number defined in Eq. (3)	
D_{diff}	Diffusivity of trace element in clinopyroxene	
EMX	Enrichment factor defined in Eq. (6)	
F	Degree of melting experienced by the solid matrix	<0.20
F_0	Reference degree of melting	0.20
k_m, k_p	Partition coefficient for the solid matrix or melting reaction	
L	Size of circular heterogeneity defined in Eq. (2)	
n	Porosity exponent in the permeability model	3
S	Relative melt suction rate	0.85–0.95
V_0	Upwelling rate of the mantle	0.1 m/yr
V_s^m, V_f^m, V_f^{ch}	Velocities of the residue, matrix melt, or channel melt	
w_p	Width of the melt pooling area	
w_{p100}	Reference width of melt pooling area	100 km
ϕ	Porosity in the matrix	
ϕ_{ref}	Reference porosity	0.01
β	A shape factor depending on grain geometry	5
Γ	Melting rate of the matrix	
ρ_f, ρ_s	Density of the melt or solid	2700 and 3300 kg/m^3
ω	Volume proportion of enriched heterogeneities	0.02–0.10
ψ	Volume proportion of channels	0.1

ing and incomplete mixing along the length of the LAB. The latter may serve as a reference model for off-axis seamounts (color-shaded region in Fig. 1a).

2.2. Disequilibrium near-fractional melting, melt migration, segregation and pooling

The governing equations are the same as those described in Liu and Liang (2017a). They consist of mass conservation equations for the matrix and channel melts and solids, Darcy's law for buoyancy driven melt segregation, and mass conservation equations for a trace element in the matrix and channel continua (Appendix A).

There are two key parameters in our melting model: relative melt suction rate (S) and melting Damköhler number (Da). S is defined as the proportion of instantaneously generated melt that is extracted to channels. When $S = 1$, all the melt generated is extracted to channels, leaving no melt porosity in the residue. This is the endmember case of perfect fractional melting. The range of S reasonable for mantle melting is 0.80–0.95 (Iwamori, 1993; Lundstrom, 2000; Liang and Peng, 2010). In this study, we use $S = 0.85$ unless stated otherwise.

The melting Damköhler number, Da, quantifies the extent of chemical disequilibrium between the residue and the percolating melt. It is defined as ratio of the rate of melting relative to the rate of diffusive exchange between the melt and residue for the element of interest (Navon and Stolper, 1987; Liang, 2003; Liang and Liu, 2016; Liu and Liang, 2017a):

$$Da = \frac{\Gamma}{\rho_s} \frac{d^2}{3\beta \cdot D_{diff}}, \quad (3)$$

where Γ and ρ_s are the melting rate and density of the residual solid, respectively; d is the average grain size; β is a shape factor; and D_{diff} is the diffusivity of the element in the mineral.

The limit of equilibrium melting is realized for the element of interest when its Da is zero. Based on inversion of REE patterns in clinopyroxene in residual abyssal peridotites, Liu and Liang (2017b) found that Da for Nd is in the range of 0–0.02. Given Da for Nd (say 0.01), Da's for other trace elements can be calculated by replacing the diffusivity of Nd in Eq. (3) by the diffusivity of the element of interest. Because the diffusion of Sr and Pb in clinopyroxene is more than four orders of magnitude faster than Nd and the diffusion of Hf in clinopyroxene is about two-thirds slower than Nd (Sneeringer et al., 1984; Cherniak, 1998; Van Orman et al., 2001; Bloch and Ganguly, 2014), Da's for Sr and Pb are effectively zero and Da for Hf is three times that of Nd. Hence, $^{87}Sr/^{86}Sr$ and $^{206}Pb/^{204}Pb$ isotope ratios of the interstitial melt and residual solid are in local chemical equilibrium whereas $^{143}Nd/^{144}Nd$ and $^{176}Hf/^{177}Hf$ isotope ratios are out of chemical equilibrium during their transit through residual peridotite in a melting column. Therefore, mantle heterogeneities as marked by isotope ratios of Sr, Pb, Nd, and Hf will experience different extent of stretching and smearing during melting and melt migration in an upwelling mantle and this effect needs to be considered in the interpretation of isotope ratios recorded in basalts and residual peridotites.

In our pseudo-2D model, the porosity and velocity in each melting column depend only on the vertical coordinate and are given by steady-state solutions of mass conservation equations for the matrix and channel continua and Darcy's law (Eqs. (A1)–(A4) in Appendix A). For the melt-

ing column directly beneath the ridge axis, the matrix porosity increases from zero to 0.53% and the matrix melt velocity increases from 0.1 m/yr to 0.56 m/yr from the solidus to the top of the 60 km-high melting column (Fig. S1).

The flux in the channel is an integral of extracted matrix melts at all depths. For efficient numerical integration of the 2D problem, we follow the simplification of Ito and Mahoney (2005a) and Wanless et al. (2014) by assuming instantaneous melt extraction through the channel:

$$\phi_{ch} V_f^{ch} C_f^{ch} = \int_0^z dz \cdot \Gamma S \frac{1-\psi}{\psi} C_f^m. \quad (4)$$

Eq. (4) is a solution for the flux of the trace element of interest in the channel melt at the top of each melting column. To calculate the composition of locally averaged melt pooled from a bundle of melting columns with height increasing from z_{min} to z_{max} toward the ridge axis, we integrate channel melt flux and matrix melt flux from the enclosed melting columns using the expression:

$$C_f^{pooled} = \frac{\int_{z_{\min}}^{z_{\max}} dz \cdot \cot\theta \cdot \left(\phi_{ch} V_f^{ch} C_f^{ch} + \phi_m V_f^m C_f^m\right)}{\int_{z_{\min}}^{z_{\max}} dz \cdot \cot\theta \cdot \left(\phi_{ch} V_f^{ch} + \phi_m V_f^m\right)}, \quad (5)$$

where θ is the slope of LAB. For constant θ, the term $\cot\theta$ can be canceled.

3. TRANSPORT AND SAMPLING OF HETEROGENEITIES

3.1. Compositions of the matrix melt

Isotope ratios of Sr, Pb, Nd, and Hf in the matrix melt vary spatially and temporally depending on the size, shape, and distribution of chemical heterogeneities in the mantle sources. This can be demonstrated through two case studies: one with a fixed size of 2.7 km and the other with a fixed size of 5.3 km (Fig. 2). The volume proportion of enriched heterogeneities in the two-component mantle source is 2.5% in both cases. For simplicity, we assume that concentrations of the incompatible trace elements (Nd, Hf, Sr, and Pb) in the enriched endmember are eight times higher than those in the depleted mantle. In a more realistic case, the relative enrichment factor may vary with element, which we will discuss in Section 4.3. Isotope ratios of Sr, Pb, Nd, and Hf in the enriched mantle correspond to those in EMII (Table 2, Stracke et al., 2003).

In the equilibrium case of $^{87}Sr/^{86}Sr$ and $^{206}Pb/^{204}Pb$ ($Da = 0$, Fig. 2(e–h)), heterogeneities are stretched vertically in the upper part of the melting region due to the vertical acceleration of the melt. The full range of isotope ratios in the source is still recorded in the matrix melt. It is possible to identify individual chemical heterogeneity in the residue, though its shape is deformed by melt-migration induced stretching. However, in the disequilibrium case of $^{143}Nd/^{144}Nd$ and $^{176}Hf/^{177}Hf$ (Fig. 2(a–d)), heterogeneities are both stretched and smeared in the upper part of the melting region where the amplitude of the enriched signal is damped. The size and extreme isotope ratios of heterogeneities in the melting region are not preserved. Heterogeneities are strongly dispersed in the upper half of the melting region, creating vertical enriched stripes. Each enriched stripe may contain more than one heterogeneity positioned closely in the vertical direction (also see Fig. S2). However, in the lower part of the melting region ($z < 20$ km), the size, shape, distribution, and amplitude of isotopically enriched signals are largely preserved, independent of the state of chemical disequilibrium. This is due to the shorter travel distance and that the effect of stretching and smearing are cumulative upward.

The distribution of chemical heterogeneities in the melting region shown in Fig. 2 is only a snapshot of the time-dependent simulations using two possible sizes of heterogeneities. In the supplementary materials, we present snapshots of two simulations with 10% enriched mantle (Fig. S2) and animations (Movies 1–4) that further illustrate the dynamic nature of melting a spatially distributed two-component mantle. The spatial distribution of heterogeneities in the melting region changes with time, though the overall picture of smearing and stretching in the upper part of the melting region are persistent.

3.2. Compositions of pooled melts

The channel melt is a vertical aggregation of matrix melt along each melting column in the triangular melting region. The matrix and channel melts emerging at the top of each melting column are assumed to be funneled to the ridge axis through the decompaction boundary layer beneath the LAB where further mixing takes place (Fig. 1). To model melt mixing beneath the LAB, we subdivide the melting region into a number of bins (one is shown as a color-shaded area in Fig. 1a) and investigate variations of isotope ratios of Sr, Nd, Pb, and Hf in locally averaged melts at different locations along the decompaction channel and as a function of the bin width. Although the physical process of mixing is not treated, locally averaged melt compositions provide useful information on the possible range of chemical variations in the pooled melts and its sensitivity to the length scale of mixing along LAB. The well-mixed pooled melt corresponds to the average melt over the entire simulation domain (i.e., a bin width of 100 km). The case of least mixing considered here has a bin width of 0.25 km, which is the cell width of the mesh.

To a first order, composition variability of pooled melt increases as the width of the melt pooling area, or the bin width, decreases or the size of heterogeneity increases (Fig. 3 and Figs. S3, S4). The ranges of $^{143}Nd/^{144}Nd$ and $^{87}Sr/^{86}Sr$ in the well-mixed pooled melt (bin width 100 km) are 15% and 22% of the two-component source when the size of heterogeneities is 2.7 km. For the same size, concentration, and proportion of enriched heterogeneities, if the bin width is reduced to 2.5 km, the pooled melts would record 43% $^{143}Nd/^{144}Nd$ and 65% $^{87}Sr/^{86}Sr$ variations in the mantle source. As the bin width decreases, the volume of individual heterogeneity relative to the melt pooling area increases, creating more variation of the pooled melt. There is a trade-off between the size of individual heterogeneity and the width of melt pooling area. The same range of isotope ratio variations can be produced by doubling the size of heterogeneity and quadrupling the

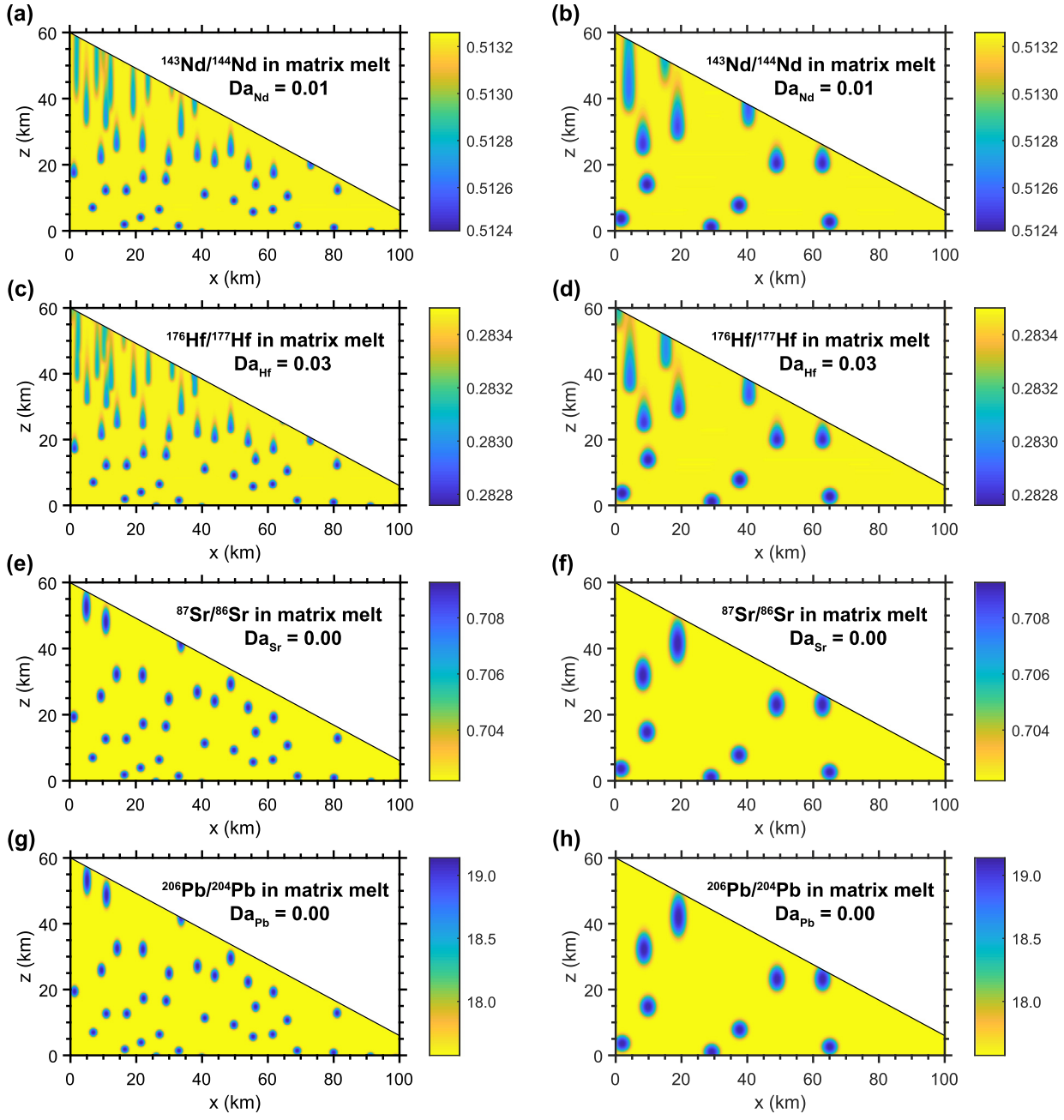

Fig. 2. A snap shot of the distribution of isotope ratios in the matrix melt in the triangular melting region produced by melting a two-component mantle that consists of randomly distributed heterogeneities. The volume proportion of enriched heterogeneities is 2.5%. The initial size of heterogeneities is 2.7 km for results presented in the left column, while the initial size is 5.3 km in the right column. The concentration of incompatible trace elements in the heterogeneity is eight times that of the concentration in the depleted-DMM of Workman and Hart (2005). The isotope ratio of the enriched endmember is calculated as EMII using the method of Stracke et al. (2003).

bin width of the melt pooling area (c.f. Fig. 3c and e). We will present a scaling relationship that can be used to compare results from different size of heterogeneity and width of melt pooling area in Section 4.4.

All else being equal, variations of $^{87}Sr/^{86}Sr$ and $^{206}Pb/^{204}Pb$ are larger than those of $^{143}Nd/^{144}Nd$ and $^{176}Hf/^{177}Hf$ when normalized by the variation of respective isotope ratio in the source (Fig. 3 and Figs. S3, S4). This difference, also observed in the mixing model of Rudge et al. (2013), is mostly due to the fact that Sr and Pb are more incompatible than Nd and Hf during mantle melting (Table 2). Consequently, the relative depletion of Nd and Hf in the shallow matrix melt produced by high degree of melting compared to that in the deep matrix melt produced by small degree of melting are less than the relative depletion of Sr and Pb. Chemical disequilibrium further hinders the depletion of Nd and Hf in the matrix melt as the degree of melting increases (Liang and Liu, 2016). The isotopically

Table 2
List of reference mantle compositions and melting parameters.

	DMM* (ppm)	EMII* (ppm)	EMX**	k_m†		*Da*
				min	max	
Ba	0.227	172.1	758	3.0×10^{-5}	1.2×10^{-4}	0.000
Nb	0.0864	4.28	49.6	0.0019	0.0029	0.000
La	0.134	9.16	68.4	0.0010	0.0072	0.020
Ce	0.421	19.7	46.8	0.0016	0.011	0.016
Pb	0.014	2.31	165	0.0019	0.012	0.000
Nd	0.483	12.7	26.2	0.0039	0.025	0.010
Sr	6.092	116.5	19.1	0.0017	0.012	0.000
Zr	4.269	72.6	17.0	0.010	0.030	0.025
Hf	0.127	2.32	18.3	0.012	0.030	0.025
Sm	0.210	3.55	16.9	0.008	0.042	0.006
Gd	0.324	4.48	13.8	0.013	0.059	0.004
Dy	0.471	5.18	11.0	0.020	0.076	0.003
Y	3.129	30.35	9.70	0.022	0.082	0.002
Yb	0.348	3.06	8.78	0.038	0.098	0.001
$^{143}Nd/^{144}Nd$	0.5133	0.5124				
$^{176}Hf/^{177}Hf$	0.2835	0.2828				
$^{87}Sr/^{86}Sr$	0.7022	0.7093				
$^{206}Pb/^{204}Pb$	17.57	19.14				
$^{207}Pb/^{204}Pb$	15.40	15.66				
$^{208}Pb/^{204}Pb$	37.20	39.71				

* DMM is the depleted-DMM from Workman and Hart (2005). The enriched endmemebr is calculated by mixing subduction-modified basalt and 25% pelagic clay recycled at 1 Ga (Stracke et al., 2003).
** Enrichment factor relative to DMM.
† The partition coefficients for minerals are from Kelemen et al. (2003), Sun and Liang (2012), and Yao et al. (2012). The melting reaction is from Kinzler and Grove (1992).

enriched melt derived from melting an enriched heterogeneity just entering the melting region will be diluted by isotopically depleted melt in the upper part of the melting region during vertical melt aggregation in the channel. The enriched isotope ratios of Sr and Pb in the melt at the bottom would be less affected by isotopically depleted melt in the upper part of the melting region. Therefore, chemical heterogeneities of Nd and Hf experience stronger vertical mixing than those of Sr and Pb during melt migration in the channel. Once the enriched signals of isotope ratios in the matrix melt travel to the upper part of the melting region, the strongly damped enriched signals of $^{143}Nd/^{144}Nd$ and $^{176}Hf/^{177}Hf$ and the strongly stretched enriched signals of $^{87}Sr/^{86}Sr$ and $^{206}Pb/^{204}Pb$ have low abundance and thus little effect on the isotope ratios of the pooled melt.

The probability density of the isotopic composition of the well-mixed pooled melt has a peak at the center of the predicted compositions which coincides with the mean composition of the mantle source on the mixing line in Fig. 3(a and d). However, the peak density is concentrated towards DMM when the bin width is smaller than 10 km (Fig. 3(b, c, e, f)). The latter happens because there is less mixing in the narrow bin and the pooled melt samples the DMM-dominated (97.5% by volume) source (see Fig. S6 for histograms of the source and the pooled melt). The sub-vertical trend that starts from DMM and gradually rotates counter-clockwise is a result of longer residence time of Nd in the melt pooling area than that of Sr (Fig. 3(c, e, and f)). Because the effective transport velocity of Sr (and Pb) in the matrix melt is faster than that of Nd (and Hf), when a Sr isotopic heterogeneity exits the melting region, the corresponding Nd isotopic heterogeneity (e.g., the smeared Nd isotopic heterogeneity beneath the axis in Fig. 2b) could be still inside the melting region and contribute to the enriched $^{143}Nd/^{144}Nd$ in the pooled melt.

In $^{143}Nd/^{144}Nd$ vs. $^{87}Sr/^{86}Sr$ diagram (Fig. 3(a and d)), the trend of the well-mixed pooled melt has a different slope than the mixing line. This counter-clockwise rotation arises because the variation of $^{87}Sr/^{86}Sr$ as a fraction of the variation in the source (22% in Fig. 3a) is larger than that of $^{143}Nd/^{144}Nd$ (15%). In the mixing model of Rudge et al. (2013), the rotation of melt trend is also observed when the "mixing parameter is large" or the mixing is relatively efficient. The rotation depends on the difference between the variation of $^{87}Sr/^{86}Sr$ and that of $^{143}Nd/^{144}Nd$ as proportions in the source, which is the consequence of aforementioned effect of different incompatibility (Rudge et al., 2013). Little or no rotation occurs if the relative isotopic variations between Sr and Nd are comparable (e.g., 39% and 34% for the case shown in Fig. 4a).

The location of the melt pooling bin within the melting region also influences the compositional variation of the pooled melt. This is illustrated in Fig. 4 and Fig. S5. The range of variations of $^{143}Nd/^{144}Nd$ and $^{176}Hf/^{177}Hf$ in bins within 50 km of the ridge axis are almost constant (also see Fig. S6). Beyond 50 km, there is an increase of the variation of $^{143}Nd/^{144}Nd$ and $^{176}Hf/^{177}Hf$ with increasing distance from the axis. For $^{87}Sr/^{86}Sr$ and $^{206}Pb/^{204}Pb$, there is no significant change in the trend of the variation as a function of bin location (Figs. S5 and S6). The insensitivity to the bin location is due to lower concentrations of incompatible

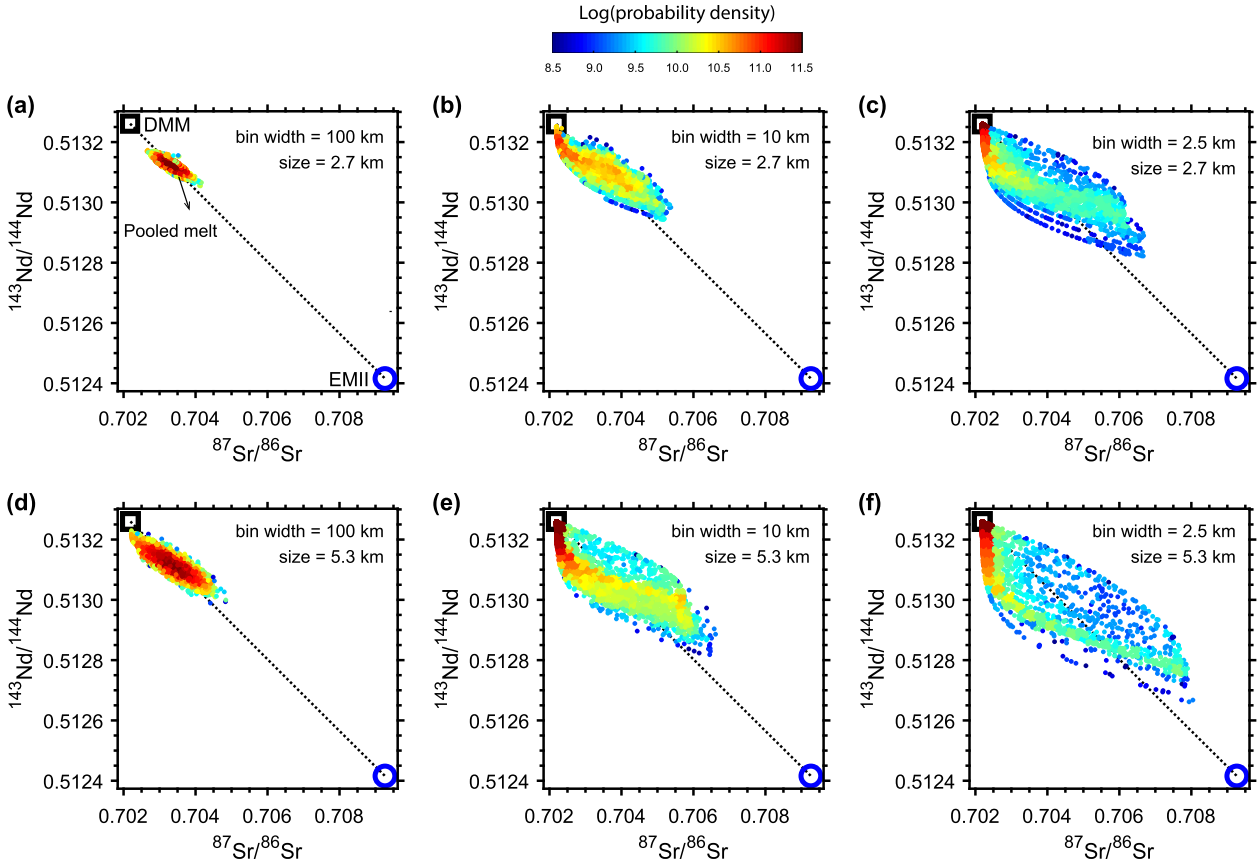

Fig. 3. Variations of isotope ratios of Sr and Nd in the pooled melt for three choices of melt pooling area and two choices of heterogeneity size. The bin width and heterogeneity size are labeled in each panel. One side of the bin is beneath the ridge axis. Colored circles represent 5000 random samples from all 20,000 samples produced by the two 60 Myr simulations. The concentrations of Nd and Sr in the enriched endmember are 8 times of the depleted mantle. The volume proportion of enriched heterogeneities is 2.5%.

trace element in the upper part of each melting column. As the distance from the ridge axis decreases, the height of the melting column and hence the extent of melting increase. Melts produced in the upper part of the melting column do not affect the pooled melt as effectively as those in the lower part. Because Nd and Hf are less incompatible than Sr and Pb, their depletions in the matrix melt are less as the degree of melting increases. Consequently $^{143}Nd/^{144}Nd$ and $^{176}Hf/^{177}Hf$ are more sensitive to the distance of the bin away from the ridge axis.

The large variation of isotope ratios in the pooled melt cannot be explained by standard mixing models in which each melt composition represents a mixed source composition or all melt compositions lie on the mixing line between melts derived from the two endmembers (Langmuir et al., 1978) for three reasons. First, the composition of the pooled melt could be outside the mixing line. Second, the trend of melt composition may not extend to the endmember compositions even if the source is a simple two-component mantle. And finally, the melt composition is diverse and governed by the static nature of the heterogeneities (size and distribution), mixing, and sampling even when the composition and proportion of endmembers are fixed. The latter is especially problematic when the number of samples is limited. For example, if one were to interpret the data of the pooled melt with $^{87}Sr/^{86}Sr$ of 0.707 in Fig. 3f or 4f as a mixture of the two-component source, the volume proportion of the enriched endmember would be 21% which is more than eight times higher than the actual proportion (2.5%). Therefore, interpreting the volume proportion of source endmember from individual melt compositions could be misleading. With spatially distributed mantle heterogeneities of specific size, it is possible to attribute samples with extreme isotope ratios as small probability event without overestimating the proportion of endmember in the two-component mantle source or invoking additional mantle component(s). Unlike the statistical parameterization for the mixing process in previous melt mixing models (e.g. Slater et al., 2001; Rudge et al., 2013), we use physical parameters such as the size of melt pooling area, and the size and elemental abundances of enriched heterogeneities to quantify the extent of mixing in Sections 4.2–4.4 below.

4. DISCUSSION

4.1. Disequilibrium melting versus equilibrium melting

Almost all geochemical studies of Nd and Hf isotope variations in partial melt produced by mantle melting use

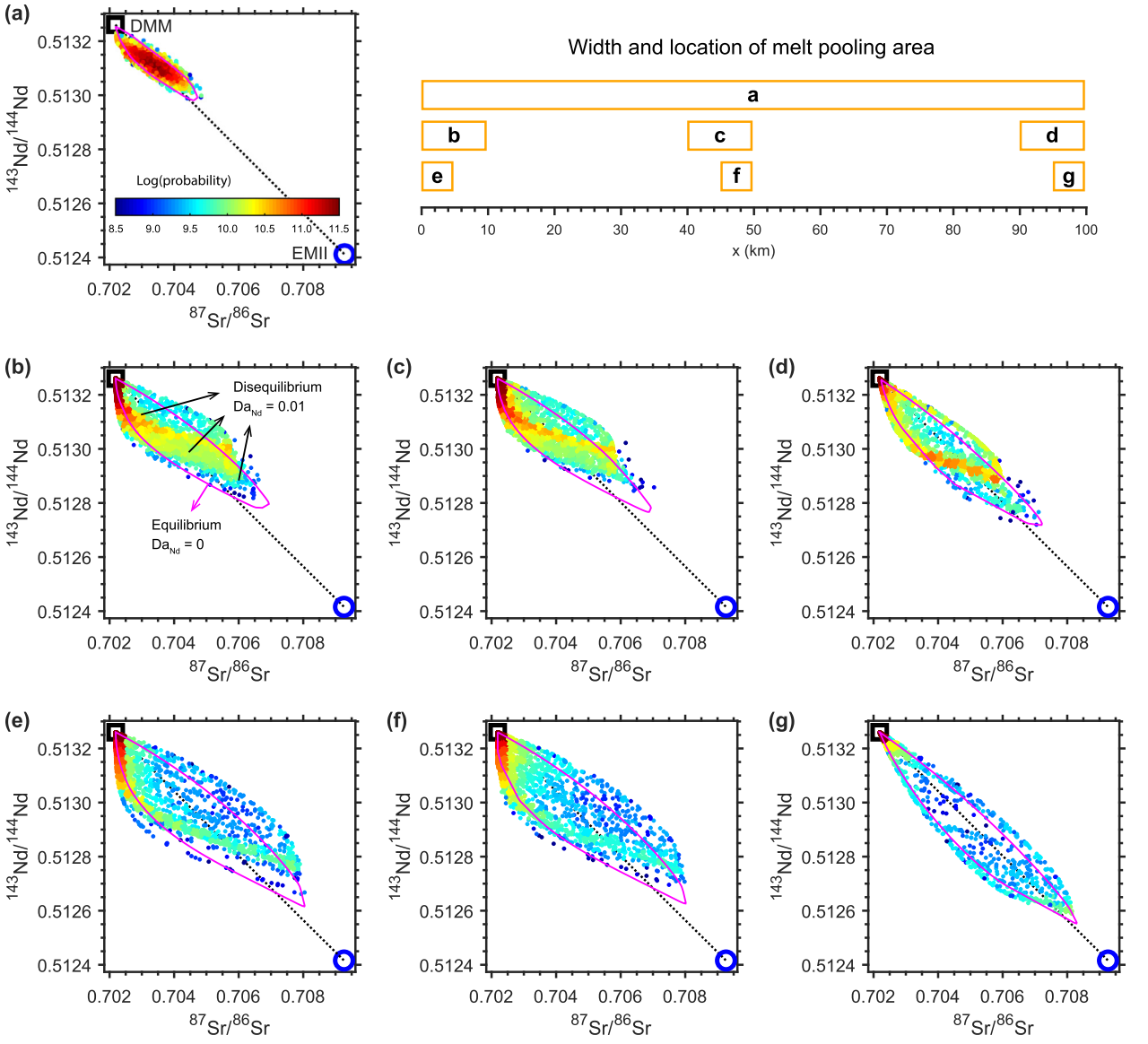

Fig. 4. Variations of $^{143}Nd/^{144}Nd$ and $^{87}Sr/^{86}Sr$ in the pooled melt for different locations of melt pooling area and bin width. The location and bin width are marked in the top right panel. Colored circles represent 5000 samples randomly picked from all 20,000 samples produced by a 60 Myr simulation. Magenta loops mark the range of melt compositions in a case of equilibrium melting ($Da = 0$). The size of heterogeneities is 5.3 km. The concentration of Nd and Sr in the enriched endmember is 8 times of the depleted mantle. The volume proportion of enriched heterogeneities is 2.5%. See supplementary Figs. S3 and S4 for isotope ratios of Pb and Hf.

an equilibrium melting model. The effect of chemical disequilibrium on Nd isotope variations in the pooled melt can be illustrated by comparing the disequilibrium case presented in Fig. 4 (color coded dots) with an equilibrium case in which we set *Da* for Nd zero (magenta loops). (Similar plots for Hf-Pb and Hf-Nd isotope ratios are shown in Figs. S3 and S4.) Depending on bin width and location, a significant fraction of melt samples in the disequilibrium case could be outside the range predicted by the equilibrium model (8% in Fig. 4a and 42% in Fig. 4b). In the case of equilibrium melting, the trend of melt compositions in the $^{143}Nd/^{144}Nd$ vs. $^{87}Sr/^{86}Sr$ correlation diagram is less rotated about the mixing line because the equilibrium bulk partition coefficient of Nd is smaller than the effective partition coefficient of Nd during disequilibrium melting (Liang and Liu, 2016). Hence, Nd and Sr behave more similar in the case of equilibrium melting. Therefore, it is important to consider chemical disequilibrium when interpreting compositional trends of the pooled melt in $^{143}Nd/^{144}Nd$ vs. $^{87}Sr/^{86}Sr$ diagram.

4.2. The effect of size distribution on the variation of isotope ratios

Results presented in Section 3 are based on simulations with uniform heterogeneity size. In a more general case, the

size of heterogeneities in the source region vary spatially. Our simulations with distributed heterogeneity size show that smaller heterogeneities are damped or dispersed more strongly and blended into the background mantle, whereas larger heterogeneities are more resistive to smearing in the upper triangular region (right column in Fig. S2). It is informative to compare variations of isotope ratios in pooled melts in cases with uniform and variable heterogeneity sizes. Fig. 5 compares temporal variations of the well-mixed pooled melts derived from three case studies: two with constant sizes (2.7 and 5.3 km) and one with non-uniform size (equal number of heterogeneities with size of 1.3 km, 2.0 km, 2.7 km, … and 6.6 km, with a volume-averaged size of 4.5 km). The width of the melt pooling area for these cases is 100 km.

The time series of isotope ratios in the well-mixed pooled melt only show low frequency fluctuations (Fig. 5). The high frequency signal produced by smaller heterogeneities in the time series of the input mantle is damped in the pooled melt. The extreme compositions in the pooled melt is preferentially set by the larger heterogeneities while smaller heterogeneities mainly contribute to the average composition of the pooled melt. We found that variations of isotope ratios of Nd and Hf in the case of variable heterogeneity size are slightly lower whereas Sr and Pb are slightly higher than the variations in the case of uniform size of 4.5 km which is the average size of the size distribution (Figs. S7 and S8). Hence it is possible to study variations of isotope ratios of Sr, Pb, Nd, and Hf in the pooled melt using the average heterogeneity size.

4.3. Trade-off between concentration and size of the enriched endmember

The abundance of the trace element in the enriched heterogeneity also affects the variation of its isotope ratio in the pooled melt. It is convenient to introduce an enrichment factor (EMX) which is defined as the concentration of the trace element of interest in the enriched endmember (C_E) relative to that in DMM (C_D):

$$\mathrm{EMX} = \frac{C_E}{C_D}. \tag{6}$$

In the examples shown in Figs. 2-5, we used a constant EMX for Nd, Hf, Sr and Pb in our simulations (EMX = 8). In a more realistic case, the enrichment factor should be element specific. In the following simulations, we set the EMX for Nd and calculate EMXs for other elements according to their elemental ratios in the enriched endmember (Table 2).

Liu and Liang (2017b) suggested that the variations of Nd and Hf isotope ratios in the pooled melt could be determined by the product of the enrichment factor and the vertical dimension of the heterogeneity which they called the enrichment strength. In their model, the shape of the enriched chemical heterogeneities is a rectangle and the width is implicitly set by the width of the melting column (11 km). To compare simulations results using different shapes of heterogeneities (e.g., circular and rectangular), we introduce the 2D enrichment strengths and the average spacing between heterogeneities:

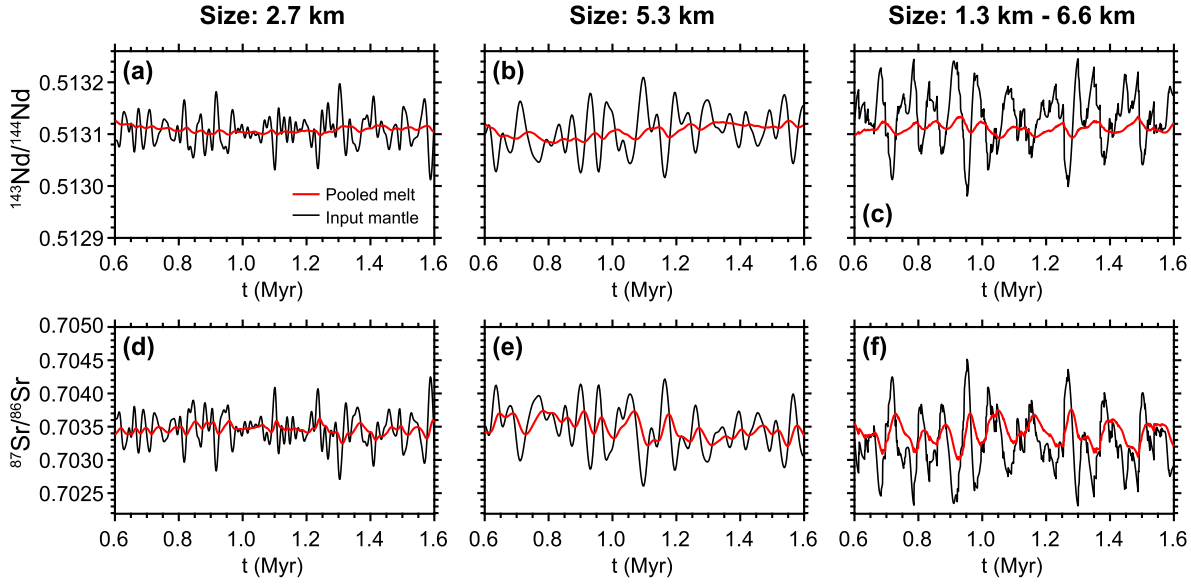

Fig. 5. $^{143}Nd/^{144}Nd$ and $^{87}Sr/^{86}Sr$ in well-mixed pooled melt as a function of time and three choices of heterogeneity size and distribution. The time series of the input mantle is the composition of the mantle averaged at the bottom of the melting region. The size or size distribution of heterogeneities is labeled above the panels. The concentration of incompatible trace elements in the heterogeneity is two times that of the concentration in the depleted mantle. The volume proportion of enriched heterogeneities is 2.5%. During the first 0.6 Myr, the number of heterogeneities in the melting region increases and the composition of the pooled melt is gradually enriched as heterogeneities start to enter. This initial burn-in stage is not shown. A snapshot of matrix melt in the case of variable size (panels c and f) is shown in supplementary Fig. S2.

$$\text{“2D enrichment strength”} = \text{EMX} \cdot A = \begin{cases} \text{EMX} \cdot \frac{1}{4}L^2\,(\text{Circle}) \\ \text{EMX} \cdot L_x L_z\,(\text{Rectangle}) \end{cases}, \quad (7)$$

$$\text{“Average spacing”} = \frac{1-\omega}{\omega} \cdot L, \quad (8)$$

where A is the effective area of the heterogeneity that accounts for the excess mass of incompatible trace element in individual heterogeneity compared to the depleted mantle; L_x and L_z are the width and height of the rectangular heterogeneity in Liu and Liang (2017b); and ω is the volume proportion of enriched heterogeneity in the two-component mantle. The size of circular heterogeneity is defined by Eq. (2).

We have calculated compositions of the well-mixed pooled melt in 30 numerical experiments with a range of sizes (0.6–10.6 km) and EMXs (2–20 for Nd). For comparison, we set the mean isotopic compositions of the two-component mantle the same in the 30 simulations. The results are summarized in Fig. 6. The enriched bound (defined as the bound of the 95% probability interval) approaches the enriched endmember as the 2D enrichment strength increases while the depleted bound approaches the depleted endmember as the average spacing between heterogeneities increases. To the first order, the range of isotope ratios in the pooled melt shrinks as the 2D enrichment strength decreases. We have obtained empirical expressions for the enriched bound and the depleted bound for the variation of isotope ratios in the well-mixed pooled melt (Eqs. (B5) and (B6) in Appendix B) and the results for $^{143}Nd/^{144}Nd$ are shown as contours in Fig. 7(a and b). The average spacing is proportional to the product of the size and the enrichment factor when the mean composition of the pooled melt is fixed. Hence the contours of enriched bound and depleted bound have slopes of −2 and −1, respectively, in the plot of EMX vs. size (Fig. 7 and Fig. S9), making it possible to estimate the size and EMXs for Nd, Hf, Sr, and Pb given the mean and standard deviation of isotope ratios of MORB. This estimation is valid for a two-component mantle source with circular-shaped heterogeneities and 100 km-wide one-sided melt pooling area.

Fig. 6a also displays results from Liu and Liang (2017b) in red shade. The isotope ratios of DMM and enriched endmembers are variable in their model. The aspect ratios (L_z/L_x) are from 0.4 to 3.2. For a 2D enrichment strength of 5 km^2, the range of variations of the pooled melt is comparable to the variation of DMM composition (gray vertical bar in Fig. 6a) although the average of the pooled melt is more enriched. Therefore, the additional variation of isotope ratios in simulations with variable DMM as the case of Liu and Liang (2017b) compared to simulations with

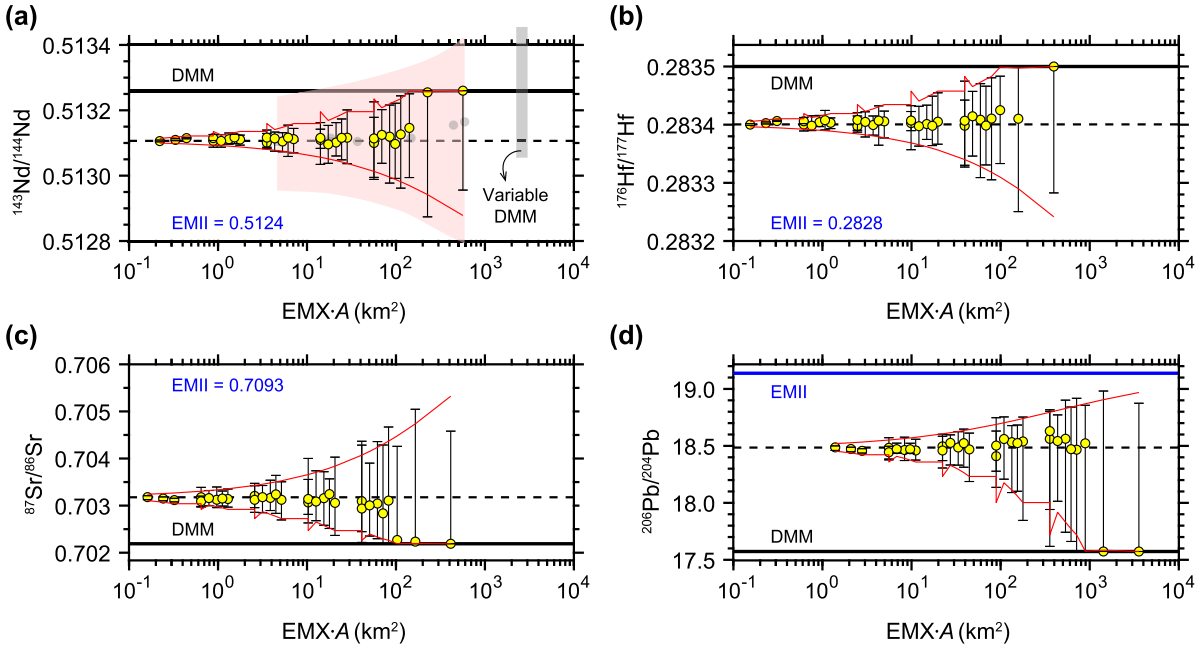

Fig. 6. Composition of the well-mixed pooled melt as a function of 2D enrichment strength. The black and blue horizontal lines mark the isotope ratios of DMM and EMII, respectively. The dashed line is the average of the source. The filled circle with vertical bars is the most probable composition and the range (95% probability interval) of the pooled melt in each simulation. The red curves are depleted and enriched bounds. The red wiggles for the depleted bound would be smoothed if the x-axis is the average spacing (see Eqs. (B5) and (B6) and discussions). Each of the 30 simulations uses at least 200 enriched heterogeneities of the same size and composition. The size of heterogeneities ranges from 0.6 to 10.6 km and the concentration of Nd in the enriched heterogeneity ranges from 2 to 20 times of DMM. Concentrations of other trace elements in the enriched heterogeneity is determined from Nd and elemental ratios in EMII (Table 2). The proportion of enriched heterogeneities in each simulation is set to assure that the average source composition is fixed. The pink shade in panel (a) is the range of pooled melt produced by variable DMM and EM compositions (Liu and Liang, 2017a). The gray box and gray circles mark the range of DMM composition and the most probable melt composition for these additional data.

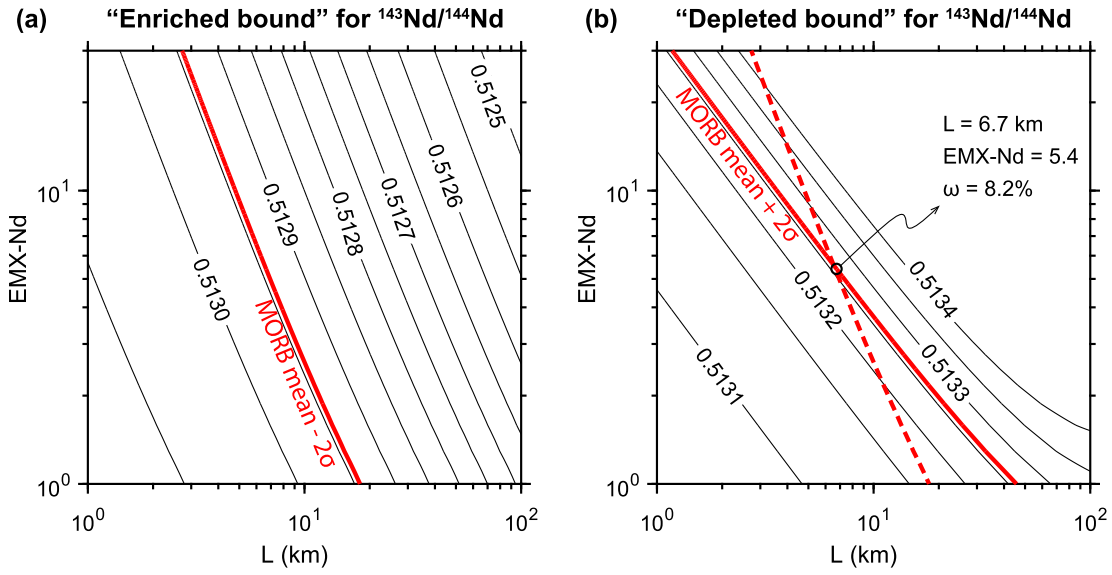

Fig. 7. The prediction of the "Enriched bound" and the "Depleted bound" of $^{143}Nd/^{144}Nd$ for the well-mixed pooled melt as functions of the size and enrichment factor of the heterogeneities (see Appendix B for details). The y-axis is the enrichment factor of Nd. The $^{143}Nd/^{144}Nd$ of the depleted mantle and the enriched endmember are 0.5134 and 0.5124 respectively. Solid red lines are the lower and upper two-standard deviation bound of $^{143}Nd/^{144}Nd$ in hotspot-unaffected MORB (compiled from PetDB, Lehnert et al., 2000). The proportion of enriched heterogeneities is restricted so that the mean $^{143}Nd/^{144}Nd$ of the pooled melt fits the mean of MORB, 0.51307. The solid red line representing the lower bound of MORB in panel (a) is copied to panel (b) as the dashed red line. The intersection in panel (b) has L of 6.7 km and EMX for Nd of 5.4. The proportion of enriched heterogeneities corresponding to the intersection is 8.2%.

constant DMM composition as the present case is probably due to the variation of DMM composition (Fig. 6a). The trend of the enriched bound and the depleted bound for variable aspect ratios of heterogeneities are parallel to the bounds for circular heterogeneities. More studies are needed to further test other choices of heterogeneity shape and aspect ratio.

4.4. Trade-off between the size of mantle heterogeneity and the size of melt pooling area

In this section, we generalize the empirical expressions of isotopic variation derived for 100 km-wide one-sided melt pooling area (Eqs. (B5) and (B6)) for the use of symmetric melt pooling areas of 5–200 km wide beneath the ridge axis. First, we compare the variation of $^{143}Nd/^{144}Nd$ in the melt pooled from a one-sided melt pooling area to that from a symmetric melt pooling area of the same width (c.f. left and right columns in Fig. 8). The solution to the symmetric melt pooling area is generated using two solutions to the one-sided melt pooling areas. The sequence of heterogeneities that enter each of the two one-sided melt pooling areas is independent of each other. Therefore, by mixing melts from these two one-sided equal-width melt pooling areas, we can produce the melt pooled from a symmetric melt pooling area. Results show that the variation of $^{143}Nd/^{144}Nd$ in the pooled melt relative to the variation in the two-component source is a function of the width of melt pooling area. The difference of relative $^{143}Nd/^{144}Nd$ variations in the pooled melt between the two cases of one-sided and symmetric melt pooling area is small if the width of the melt pooling area is the same (each row of Fig. 8).

Next, we quantify the trade-off between the size of mantle heterogeneity and the size of melt pooling area. To produce the *same* $^{143}Nd/^{144}Nd$ variations in the melt pooled from a melt pooling area narrower or wider than 100 km using Eqs. (B3)–(B6), one would need to replace the true size (L) with an equivalent size (L^*) in accordance to the size of melt pooling area. We have inverted for the equivalent size for a fixed true size of heterogeneities (5.3 km) and a range of width of melt pooling areas (2.5–200 km) and plotted the equivalent size against the width of melt pooling area in Fig. 9. There is a negative correlation between the equivalent size, L^*, and the width of melt pooling area, w_p. This correlation can be well fitted with $L^* \sim w_p^{-1/2}$ for w_p from 2.5 km to 100 km, although the correlation conforms to $L^* \sim w_p^{-1}$ better if w_p is greater than 100 km (Fig. 9). For simplicity, we use $L^* \sim w_p^{-1/2}$ (Eq. (B7)) for w_p from 2.5 km to 200 km because the misfit at $w_p = 200$ - km is only 1 km which is acceptable. The square root dependence emphasizes the importance of the area (volume in 3D) of the heterogeneity in the melt pooling area. The concentration of incompatible elements in the upper part of the melting region is low. Consequently, the effective volume of the melting region is proportional to the width of the melting region. Hence the empirical scaling relationships Eqs. (B5) and (B6) in Appendix B is further generalized by normalizing the volume of the heterogeneity ($\sim L^2$) to the effective volume of the melting region ($\sim w_p$) through Eq. (B7). The usefulness of the empirical scaling relationships is demonstrated below.

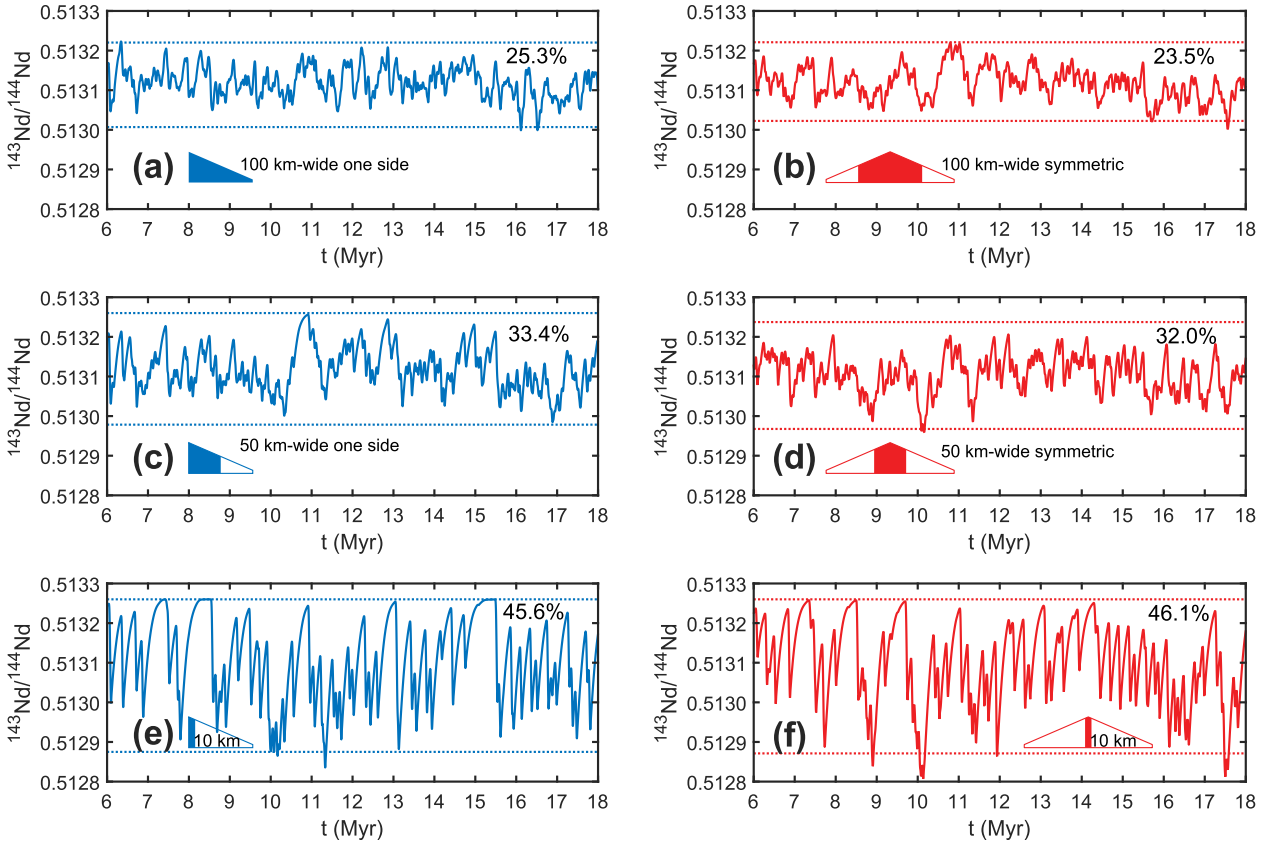

Fig. 8. Comparison of the temporal variation of $^{143}Nd/^{144}Nd$ in the melt pooled from a one-sided melt pooling area (a, c, e) versus that from a symmetric melt pooling area of the same width (b, d, f). The size of heterogeneities is 5.3 km. The volume proportion of heterogeneities is 2.5%. EMX for Nd is 8. The Damköhler number for Nd is 0.01. Dashed lines mark the 95% probability interval of all melts in a 60-Myr simulation (only a 12-Myr time series is shown). The proportion of the 95% probability interval relative to the range of $^{143}Nd/^{144}Nd$ in the two-component source is labeled in each panel.

4.5. Application to isotope ratios of MORB

Using a 100 km-wide melt pooling area and specific choice of endmember isotope compositions, one can estimate the size and EMXs of enriched heterogeneities that are responsible for the mean and standard deviation of isotope ratios of MORB (Fig. 7 and Fig. S9). As an example, let the enriched bound be the mean $^{143}Nd/^{144}Nd$ in global MORB (not affected by hotspots) minus two standard deviations (red dashed line in Fig. 7b) and the depleted bound be the mean $^{143}Nd/^{144}Nd$ in global MORB plus two standard deviations (red solid line in Fig. 7b). The intersection of these two red lines in Fig. 7b means that the variation of $^{143}Nd/^{144}Nd$ in hotspot-unaffected global MORB can be reproduced by melting a two-component mantle with 8.2% volume proportion of enriched heterogeneities that have 5.4 times higher abundance of Nd compared to the depleted mantle and an average size of 6.7 km (Fig. 7).

In supplementary Fig. S9 we provide estimates for the size and enrichment factor suitable for the means and standard deviation of $^{176}Hf/^{177}Hf$, $^{87}Sr/^{86}Sr$, and $^{206}Pb/^{204}Pb$ in global MORB not affected by hotspots. The estimated size ranges from 5.1 to 6.7 km while the proportion of enriched heterogeneities ranges from 5.2% to 8.2%. This result is confirmed by a forward simulation using size and proportion of enriched heterogeneities from the estimated range (Fig. 10). A more robust inversion should consider the uncertainty in the endmember isotope compositions and utilize constraints from all available isotope ratios simultaneously to deduce a consistent estimation of the size and volume proportion of enriched heterogeneities.

The isotope ratios of the pooled melt scatter around the mean composition of MORB (Fig. 10). In $^{143}Nd/^{144}Nd$ vs. $^{87}Sr/^{86}Sr$ and $^{176}Hf/^{177}Hf$ vs. $^{143}Nd/^{144}Nd$ diagrams (Fig. 10(a and b)), the scattered trends of the melts form elongated oval shapes that rotate counter-clockwise and clockwise, respectively, about the local slope of the mixing line at the mean composition. The sense of rotation is consistent with previous simulations with constant EMXs for all elements, further confirming the importance of incompatibility of trace elements on controlling the extent of variations in the isotope ratios relative to that in the source (Section 3.2). The quasi-linear trend of the melt does not necessarily require a linear mixing line between the two endmembers in the source, i.e. the same EMX for the two elements in the x and y axes of the isotope ratio diagram. The melt trend should not be simply extrapolated in search for the isotopic composition of the endmember in the source.

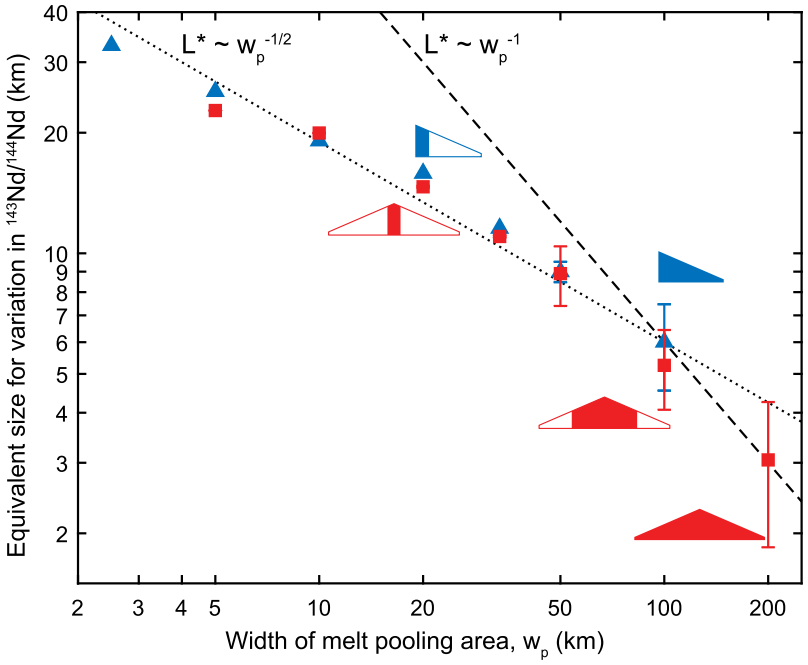

Fig. 9. The equivalent size for variation in $^{143}Nd/^{144}Nd$ as a function of the width of the melt pooling area. The size of heterogeneity is 5.3 km. Narrower melt pooling area produces larger variation in $^{143}Nd/^{144}Nd$, thus larger equivalent size. The half-space melt pooling area (blue symbols) has similar equivalent size as the symmetric melt pooling area (red symbols) of the same width. Two lines of different scaling relationships ($w_p^{-1/2}$ and w_p^{-1}) are shown for reference. (For interpretation of the references to colour in this figure legend, the reader is referred to the web version of this article.)

Nevertheless, when plotting isotope ratios of the same element, such as $^{207}Pb/^{204}Pb$ vs. $^{206}Pb/^{204}Pb$, the trend of the melt lies on the mixing line of the two-component source (Fig. 10(c and f)).

If the width of the melt pooling area narrows, the isotopic variation in the pooled melt is larger for the same 5.3 km heterogeneities (loops and braces in Fig. 10). A melt pooling width of 25 km produces 60%, 82%, 100%, and 66% more variation in $^{87}Sr/^{86}Sr$, $^{143}Nd/^{144}Nd$, $^{176}Hf/^{177}Hf$, and $^{206}Pb/^{204}Pb$ than those of a melt pooling area of 100 km wide. Based on the scaling relationship between the size of the heterogeneity and the width of melt pooling area, the size of heterogeneity responsible for the standard deviation of MORB could be 3.7 km if the melt pooling area is 50 km wide (using Eq. (B7)). Therefore, to estimate the size of mantle heterogeneity one must know the width of the melt pooling area. The latter depends on the mechanism of melt migration in and around LAB. The variations of melt pooling area under different ridge settings will propagate into the uncertainty of the estimate of the size of heterogeneities.

The current simulation cannot reproduce some MORB data with relatively low $^{143}Nd/^{144}Nd$ at given $^{87}Sr/^{86}Sr$, high $^{176}Hf/^{177}Hf$ at given $^{143}Nd/^{144}Nd$, and high $^{207}Pb/^{204}Pb$ at given $^{206}Pb/^{204}Pb$ (Fig. 10). Lack of these isotopic signatures could be due to the limitation of the two-component source which consists of DMM and an EMII-flavored component. Introducing additional enriched endmembers, such as EMI, HIMU, and/or FOZO, could produce more variations in these isotope ratio diagrams. In supplementary materials, we provide one such example for melting a five-component mantle (Fig. S10). The variations of melt compositions in $^{207}Pb/^{204}Pb$ vs. $^{206}Pb/^{204}Pb$ diagrams (e.g. Saal et al., 1998) would also require at least three endmembers in the source. The depleted endmember could also be variable and include the ultra-depleted mantle source (Liu et al., 2008; Sanfilippo et al., 2019).

The eruptible melt at the ridge axis could be an incomplete mixture of melts pooled from different melting columns stacked laterally from the axis. The range of isotope ratios in the melt erupted at the ridge axis could extend to the range of chemically extreme melts pooled from the narrowest and furthest melting column (e.g., magenta loops in Fig. 10(d-f)). These chemically extreme melts have a small volume flux compared to the total melt flux at the ridge axis, and hence may not be routinely sampled. Therefore, there could be a few samples with isotope ratios beyond the two-standard deviations of the eruptible melt at the axis. In the next section, we show that the abundances of incompatible trace elements are also sensitive to the location of the melt pooling area and can be used to further constrain the extent of incomplete mixing.

4.6. Incompatible trace elements

The pseudo-2D ridge model can also be used to understand variations of incompatible trace element concentrations in MORB. Fig. 11a shows the variation of trace element patterns of MORB with more than 6 wt% MgO and not affected by hotspots (Lehnert et al., 2000). We sug-

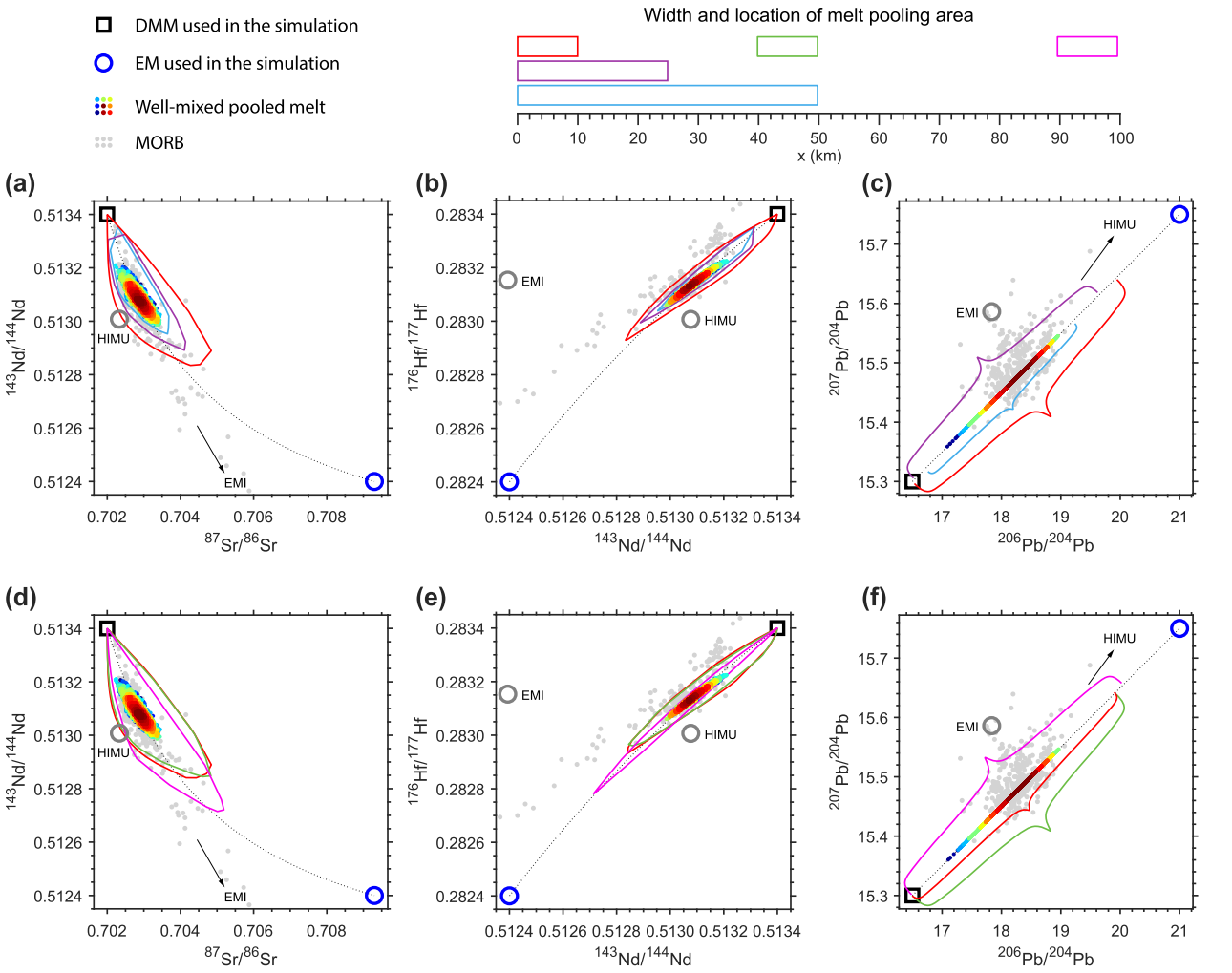

Fig. 10. Comparison of the pooled melt and MORB not influenced by hotspots in isotope ratio diagrams. The size of enriched heterogeneities is 5.3 km and the volume proportion of enriched heterogeneities is 6%. The EMXs for Nd, Hf, Sr, and Pb are 7.4, 5.6, 2.2 and 10.4, respectively. Color filled circles are samples of well-mixed pooled melt. The range of locally pooled melt is superimposed as colored loops. MORB data are shown as gray dots (compiled from PetDB, Lehnert et al., 2000). Dotted lines are mixing lines between DMM and the enriched endmember used in the simulation.

gest that such large variation is likely due to incomplete mixing of melts pooled from melting columns of different heights. The variation of incompatible trace element concentrations in the source could be homogenized in the well-mixed pooled melt. In the calculation shown in Fig. 11, the enriched endmember has eight times higher Nd abundance than DMM. However, there is only 20% relative variation of Nd in the well-mixed pooled melt. The 1/40 reduction of source variation would make source variation due to any enriched endmember barely visible in the Nd abundance of the well-mixed pooled melt. Therefore, variations of incompatible trace elements in the enriched endmember are significantly damped in the well-mixed pooled melt, by melt migration induced mixing along the melting column and lateral mixing along LAB.

The small variation of well-mixed pooled melt cannot be effectively enhanced by using variable DMM composition as the variation of incompatible trace element concentration in depleted mantle is only five times for Ba and 20% for Yb (Workman and Hart, 2005). The variation of well-mixed pooled melt could hardly reach the magnitude of variations in MORB even if we consider the largest possible size in the previous section (6.7 km). Our simulations suggest that melts derived from melting columns of different height could produce significantly larger variation of incompatible trace element abundances than the well-mixed pooled melt (Fig. 11c). Concentrations of incompatible trace elements increase with increasing distance away from the ridge axis or decreasing height of the melting column, whereas variations of the trace elements in a given melting column increases with their incompatibility. Collectively, the incompletely mixed melts from various distance away from the ridge axis could have 500 times of variation in Ba and five times of variation in Yb (Fig. 11c).

In our model, the channel melt mixes with the matrix melt at the top of the 1D melting column. However,

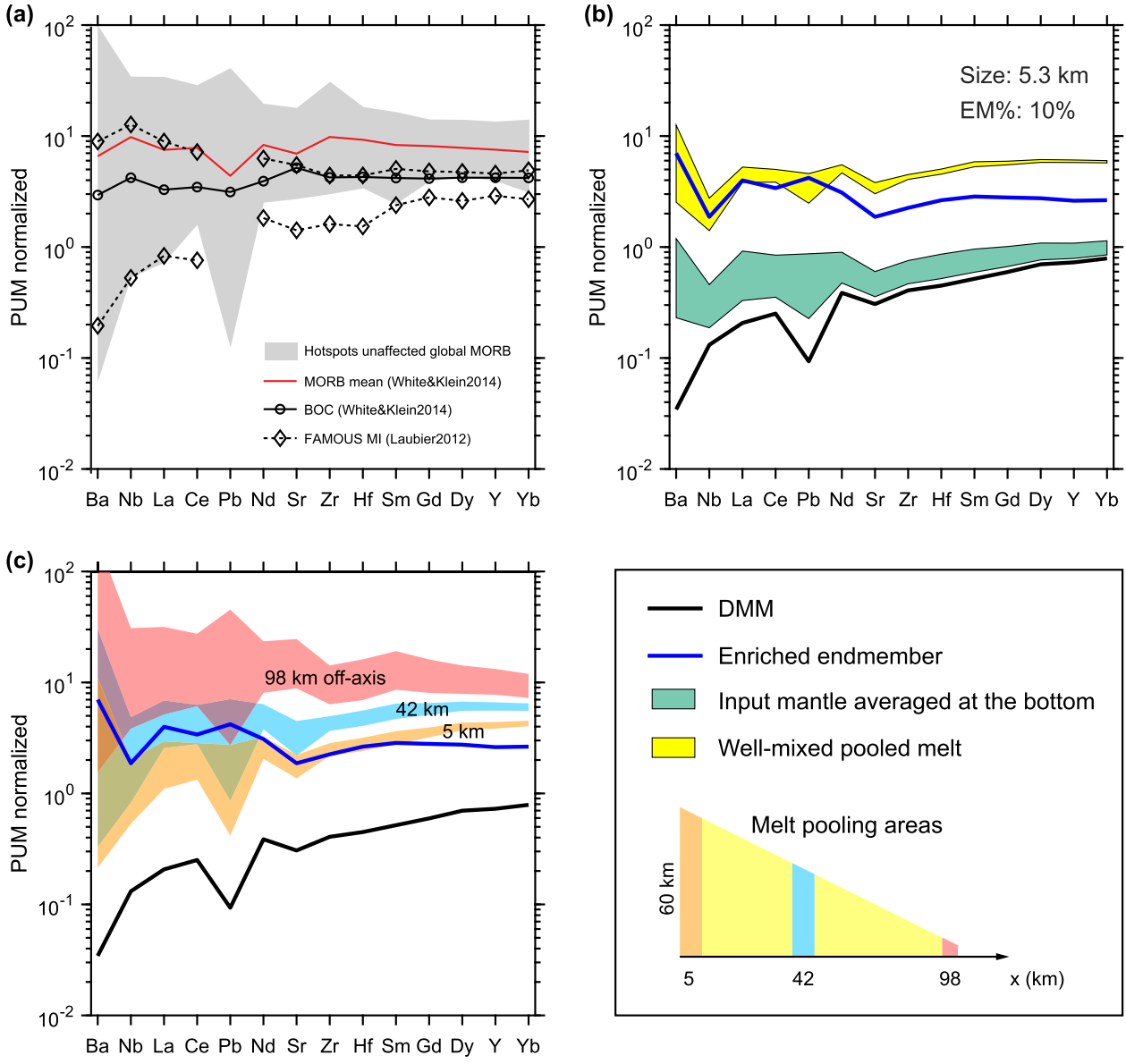

Fig. 11. Comparsion of trace element patterns of the well-mixed pooled melt and off-axis melts with observations of MORB, bulk oceanic crust, and olivine-hosted melt inclusions. The width of the two bins 5 km and 42 km off axis is 10 km while the bin 98 off axis is 7 km wide. The concentration is normalized by primitive upper mantle (McDonough and Sun, 1995). The elemental ratio of the enriched endmemeber is caculated by the method of Stracke et al. (2003). The range of trace element patterns of hotspot-unaffected global MORB (MgO > 6%) is compiled from PetDB database (Lehnert et al., 2000). The dataset has excluded samples within 800 km of any hotspot recognized by Courtillot et al. (2003). The MORB mean is from White and Klein (2014). The range of melt inclusion data from the FAMOUS segment only includes high-MgO melt inclusions hosted by olivines (Laubier et al., 2012).

Spiegelman and Kelemen (2003) reported large variation of incompatible trace element abundances in the melt sampled at the top on the scale of one channel width. The width of dunite channels observed in the field has a skewed probability distribution weighted toward the lower end of the spectrum from 0.1 m and 200 m (Kelemen et al., 2000). Such small-scale variability in the melt is likely to be homogenized in the axial magma chamber (DePaolo, 1996) and may not provide a viable mechanism to produce the observed variation of incompatible trace element abundances in MORB. Assuming a volume of axial magma chamber of 1 km^2 per length of the ridge (Sinton and Detrick, 1992), the width of the melting column must be at least 10 km for the melt flux pooled from the melting column to endure homogenization in the axial magma chamber.

Crustal level fractionation is unlikely a major factor responsible for the incompatible trace element variability observed in MORB samples with more than 6% MgO (only a factor of two along the liquid line of descent, White and Klein (2014)). The effect of along-ridge variation in the degree of melting can be filtered out by excluding hotspots

affected ridges or considering primitive melt inclusions collected at a local ridge segment (Laubier et al., 2012). The large variation of incompatible trace element ratios, such as $(La/Sm)_N$, could also be attributed to incomplete mixing along LAB (Fig. S11). Therefore, the large variation of incompatible trace element abundances in MORB provides strong evidence for incomplete mixing of locally pooled melts, which is consistent with other mixing models for trace elements, isotope ratios, and U-series (e.g., Slater et al. 2001; Stracke et al., 2006; Rudge et al., 2013).

5. SIMPLIFICATIONS AND PERSPECTIVES

The pseudo-2D two-porosity ridge model expands previous geochemical treatment of decompression melting beneath mid-ocean ridges (O'Hara, 1985; Holness and Richter, 1989; Plank and Langmuir, 1992; Asimow and Langmuir, 2003; Wanless et al., 2014; Liu and Liang, 2017b) by considering disequilibrium melting and melt transport in residual matrix, channelized melt migration, and spatially and temporally variable mantle source compositions. Nonetheless, our bundle of column model is simplified. In particular, the flow of the residue mantle and the matrix melt in the triangular melting region is vertical. In a more realistic case of corner flow and melt focusing where streamlines of the matrix melt and solid are different in the upper part of the melting triangle (e.g. Phipps Morgan, 1987; Spiegelman and McKenzie, 1987; Keller et al., 2017; Liu, 2018; Liu and Liang, 2019), chemical heterogeneities would be rotated and further deformed during their transit through the melting region. This corner flow-induced effect is important for the interpretation of isotope ratios and incompatible trace element variations in the residual solid. However, variations of Sr, Pb, Nd, and Hf isotope ratios in the pooled melt would not be significantly affected by horizontal melt transport near the ridge axis. As we discussed in Section 3.2, melts produced in the upper part of the triangular melting region have considerably lower incompatible trace element abundances (due to preferential partitioning into the melt), and hence exert less control on the variation of Sr, Pb, Nd, and Hf isotope ratios in the pooled melt than melts derived from the lower part of the melting region.

In the current simulation of melt mixing at LAB, we did not consider melt transport within the decompaction boundary layer, which is likely more complicated and results in additional mixing of melts emerging at different locations in the decompaction channel (Ghods and Arkani-Hamed, 2000). The pooled melt at any given time could be an ensemble of LAB melts at all distance but with different weights/probabilities. Although LAB melts will eventually enter the axial magma chamber, the erupted melt could still inherit some chemical variations due to a local melt pooling area that is wider than 10 km but much smaller compared to the entire melting region. It would be a worthwhile future study to investigate the mixing of LAB melts as they enter the decompaction channel and are transported toward the ridge axis.

Another simplification of the present study is the constant relative melt suction rate, S, in the 2D melting region. Values of S that can explain variations of REE abundance in residual clinopyroxene in abyssal peridotites is in the range of 0.8 to 0.95 with the latter representing near perfect fractional melting (Iwamori, 1993; Lundstrom, 2000; Liang and Peng, 2010). Increasing the value of S from 0.85 used in the present study to 0.95 results in slightly larger variations in $^{87}Sr/^{86}Sr$ and $^{143}Nd/^{144}Nd$ (Fig. S13) and negligible variation of incompatible trace element abundances (Fig. S12) in the pooled melt. The effect of S is secondary to the enrichment strength and the effect of size of the melt pooling area. Therefore, corrections for S in the quantitative estimate of the variation in isotope ratios is not included in the present model.

The chemical heterogeneity considered in the present study has the same lithology and melting rate as the depleted background mantle. This simplification allows us to avoid complications such as porosity waves, time-dependent flow fields, and pyroxenite-derived melt and lherzolite or harzburgite reaction (see Liang and Liu, 2018 for further discussion). These complicated and not well constrained effects were avoided in previous modeling of melting a lithologically heterogeneous mantle by assuming no chemical interaction between melt derived from one lithology with melt and solid in another lithology (e.g. Ito and Mahoney, 2005a, b; Stracke and Bourdon, 2009; Rudge et al., 2013). The difference in solidus and melt productivity of lithologically distinct components in the mantle could affect the melt composition if the final melting depth is variable (Ito and Mahoney, 2005a). The size and spatial distribution of enriched chemical and lithological heterogeneities may be linked to the formation of high-porosity (dunite) channels in an upwelling melting region (e.g. Schiemenz et al., 2008; Liang et al., 2010; Liang et al., 2011; Weatherley and Katz, 2016; Keller et al., 2017), although the physical processes and petrological and geochemical consequences of the interaction between pyroxenite-derived melt and peridotites remain poorly constrained.

The present model examines the spatial and temporal variations of chemical heterogeneities in a 2D section. However, the majority of MORB samples are collected along ridge and time series or ridge-transverse samples are rare (e.g. Cordier et al., 2010). The MORB sample may be regarded as a snapshot in the time series of the melt pooled from a 3D melt pooling region. If the vertical and lateral distributions of the heterogeneities are statistically similar, the along-ridge MORB samples may be regarded as random samples in the time series of the pooled melt. If there are vertical and lateral anisotropy in the distribution of mantle heterogeneity in the mantle source, caution should be exercised when comparing along-ridge variations of isotope ratios and incompatible trace element in MORB samples with time series results based on 2D time-dependent ridge models.

6. CONCLUSIONS

We have examined the variations of isotope ratios of Sr, Pb, Nd, and Hf and selected incompatible trace elements in pooled melts produced by disequilibrium melting and melt

transport in a spatially and chemically heterogeneous mantle beneath mid-ocean ridges using the pseudo-2D two-porosity model. An important new feature of our pseudo-2D ridge model is that the mantle source composition varies both spatially and temporally during melting. Through numerical examples and simple analysis, we have demonstrated the importance of the size and distribution of mantle heterogeneities, the elemental abundance of enriched heterogeneities, and the width of melt pooling area to the interpretation of isotope ratios and incompatible trace elements in basalts erupted on the surface. The main results of this study can be summarized as follows:

1. Compositions of the matrix melt vary spatially and temporally depending on the size and spatial distribution of chemical heterogeneities in the mantle sources. The enriched signals marked by isotope ratios of Sr and Pb in the matrix melt are stretched along melt flow direction in the upper part of the melting region and their amplitudes in the mantle source are preserved in the matrix melt and solid. The enriched signals marked by isotope ratios of Nd and Hf in the matrix melt are both stretched and smeared in the upper part of the melting region and their amplitudes are damped due to the finite rate of chemical exchange between the matrix melt and the minerals. The size and extreme isotope ratios of Nd and Hf in the melting region are not preserved. These element-dependent stretching and smearing arise naturally during decompression melting of a heterogenous mantle and are fundamental to the interpretation of variations of isotope ratios in the pooled melt, residual solid, and the mantle source.
2. Compositions of the pooled melt are mixtures of the channel melt and matrix melt sampled in part of the decompaction boundary layer beneath the LAB. In general, composition variability of pooled melt increases with the increase of heterogeneity size and the decrease of the width of the melt pooling area. The same range of isotope ratio variations can be produced by doubling the size of heterogeneity and quadrupling the bin width of the melt pooling area.
3. Based on results of numerical simulations, we quantified the trade-offs between the size of enriched blob and the abundances of Sr, Nd, Pb, and Hf in the enriched mantle, and between the size of the blob and the width of melt pooling area using "2D enrichment strength" and "equivalent size", respectively. Using a 100 km-wide melt pooling area, the standard deviation and mean of $^{143}Nd/^{144}Nd$, $^{176}Hf/^{177}Hf$, $^{87}Sr/^{86}Sr$, and $^{206}Pb/^{204}Pb$ in global MORB not affected by hotspots can be reproduced by melting a two-component mantle with 5.2–8.2% enriched heterogeneities of 5.1–6.7 km mean size and 7.0($\pm$1.6), 5.3($\pm$1.2), 2.0($\pm$0.5), and 9.8($\pm$2.2) times higher abundances of Nd, Hf, Sr, and Pb than the depleted mantle, respectively. Melts pooled far away from the ridge axis could explain some isotope ratios outside the standard deviation.
4. Using the time-dependent pseudo-2D two-porosity model, we show that variations of $^{87}Sr/^{86}Sr$ and $^{206}Pb/^{204}Pb$ in pooled melt are larger than variations of $^{143}Nd/^{144}Nd$ and $^{176}Hf/^{177}Hf$ in pooled melt when normalized by the variation of respective isotope ratio in the mantle source. The trend of the well-mixed pooled melt is rotated counter-clockwise in $^{143}Nd/^{144}Nd$ vs. $^{87}Sr/^{86}Sr$ diagram, resulting in a different slope than the mixing line. Depending on the size and volume proportion of heterogeneity and the melt pooling area, the interception of the two trends may not coincides with the mean composition of the mantle source and the extreme isotope ratios of the pooled melt may not sample the depleted and enriched endmember components of the mantle source. These systematic variations in radiogenic isotope ratios in the pooled melt are broadly similar those observed in the statistical mixing model of Rudge et al. (2013) for melting a lithologically heterogeneous mantle, underscoring the importance of mixing in producing compositional variations in eruptible melts.
5. The variation of incompatible trace element abundance in the two-component mantle is significantly reduced in the well-mixed pooled melt. Melts pooled from melting columns further away from the ridge axis could have more than a factor of 10 higher concentration of incompatible trace elements than the well-mixed pooled melt. The large variation of incompatible trace element abundances in MORB suggests that the mixing of melts during lateral focusing is incomplete. More studies are needed to quantify the process of melt transport in the decompaction boundary layer beneath LAB.

The present study highlights the need of knowledge on the size, shape, and spatial distribution of mantle heterogeneities in the source region of basalts. These physical properties of the mantle source, as well as composition and lithology, are ultimately controlled by mantle convection, slab recycling, and crust formation processes (e.g. Morgan and Morgan, 1999). By considering the size and spatial distribution of mantle heterogeneity in the basalt source region and melting and migration processes, it is possible to make better connection between mantle geochemistry and geodynamics (e.g. Gurnis and Davies, 1986).

7. RESEARCH DATA

Research Data associated with this article can be access at https://doi.org/10.17632/tprnvr5w25.1

Declaration of Competing Interest

The authors declare that they have no known competing financial interests or personal relationships that could have appeared to influence the work reported in this paper.

ACKNOWLEDGEMENTS

This paper is benefited from thoughtful reviews by Garrett Ito, Andreas Stracke, and two anonymous reviewers. We are indebted to Garrett Ito for drawing our attention to the relative size of the enriched blobs to the size of the melt pooling area, which led to the discussion in Section 4.4. This work was supported by National

Science Foundation grants EAR-1624516 and OCE-1852088, and a Brown University dissertation fellowship.

APPENDIX A. GOVERNING EQUATIONS

Solutions of matrix porosity, matrix melt velocity, and the channel melt flux are required before solving the conservation equations for the trace element. In one-dimension, the evolution of the physical state of the melting column are governed by the following equations (Iwamori, 1993; Lundstrom, 2000; Jull et al., 2002; Liang and Parmentier, 2010):

$$\frac{d\left(\rho_f \phi V_f^m\right)}{dz} = \Gamma(1-S), \tag{A1}$$

$$\frac{d\left[\rho_s(1-\phi)V_s^m\right]}{dz} = -\Gamma, \tag{A2}$$

$$\frac{d\left(\rho_f \phi V_f^{ch}\right)}{dz} = \frac{1-\psi}{\psi}\Gamma S, \tag{A3}$$

$$\phi\left(V_f^m - V_s^m\right) = \frac{k_\phi}{\eta_f}(1-\phi)\Delta\rho g, \tag{A4}$$

where Eqs. (A1)–(A3) are mass conservation equations for the matric melt, matrix solid, and channel melt. Eq. (A4) is Darcy's law. We solve the above equations using the method of Liang and Liu (2018). The solutions are given below:

$$\phi_m = \frac{(1-S)F_0 V_0 \cdot z}{V_f^m}, \tag{A5}$$

$$V_f^m = (1-S)^{2/3} \cdot \frac{F_0 V_0}{\phi_{ref}} \cdot z + (1-z)\cdot V_0, \tag{A6}$$

$$V_s^m = \frac{(1-F_0\cdot z)\cdot V_0}{1-\phi}, \tag{A7}$$

$$\phi_{ch} V_f^{ch} = F_0 V_0 \cdot S\frac{1-\psi}{\psi}\cdot z, \tag{A8}$$

where ϕ_{ref} is the reference porosity at the top of the melting column if there is no melt extraction (Liang and Liu, 2018); F_0 is the reference degree of melting, 0.2; V_0 is the upwelling rate of the mantle. In the current model, we set ϕ_{ref} to be 0.01. In deriving Eq. (A6), we assume constant melting rate and linear velocity profile for the matrix melt. The velocity of the matrix melt at the top of the melting column is constrained by Darcy's law and mass conservation (Liang and Liu, 2018).

To model spatially distributed mantle heterogeneities in the melting region, we use the following time-dependent mass conservation equations for a trace element in the matrix melt, matrix solid, and channel melt:

$$\frac{\partial\left(\rho_f \phi_m C_f^m\right)}{\partial t} + \frac{\partial\left(\rho_f \phi_m V_f^m C_f^m\right)}{\partial z} = \Gamma\frac{k_p}{k_m}C_s^m - \Gamma S C_f^m + \rho_s(1-\phi_m)\frac{3\beta\cdot D_{diff}}{d^2}\left(C_s^m - k_m C_f^m\right), \tag{A9}$$

$$\frac{\partial\left[\rho_s(1-\phi_m)C_s^m\right]}{\partial t} + \frac{\partial\left[\rho_s(1-\phi_m)V_s^m C_s^m\right]}{\partial z} = -\Gamma\frac{k_p}{k_m}C_s^m - \rho_s(1-\phi_m)\frac{3\beta\cdot D_{diff}}{d^2}\left(C_s^m - k_m C_f^m\right), \tag{A10}$$

$$\psi\frac{\partial\left(\rho_f \phi_{ch} C_f^{ch}\right)}{\partial t} + \psi\frac{\partial\left(\rho_f \phi_{ch} V_f^{ch} C_f^{ch}\right)}{\partial z} = (1-\psi)\Gamma S C_f^m. \tag{A11}$$

where ψ is the volume proportion of channels; z is the vertical distance above the solidus; ϕ is porosity; V is velocity; C is concentration; superscript/subscript m and ch refer to the matrix and the channel; superscript/subscript s and f refer to the solid and the melt; k_m is the bulk partition coefficient; k_p is the partition coefficient calculated according to melting reaction.

In Eq. (A11) we neglected the partitioning of incompatible trace element in olivine in the dunite channel, as Sr, Pb, Hf, and REE are highly incompatible in olivine. The sum of Eqs. (A9)–(A11) recover the global mass conservation equation for the matrix and channel continua. For simplicity, we assume that the volume proportion of channels is uniform in the melting region. The first term on the right-hand side (RHS) of Eqs. (A9) and (A10) describe melting of the matrix. The third term on RHS of Eq. (A9) and the second term on RHS of Eq. (A10) are due to diffusive exchange between the mineral and melt in the matrix continuum. The second term on RHS of Eq. (A9) and the RHS of Eq. (A10) describe extraction of matrix melt into the channel.

To solve the time-dependent Eqs. (A9) and (A10) numerically, we first nondimensionalize the governing equations using the height of the melting column beneath the ridge axis as the length scale and the solid upwelling time as the time scale.

For convenience of numerical integration using a high-order accurate method, we introduce two conserved variables:

$$C_f^{m'} = \phi_m C_f^m, C_s^{m'} = (1-\phi_m)C_s^m. \tag{A12}$$

The nondimensionalized equations then become

$$\frac{\partial\left(C_f^{m'}\right)}{\partial t} + \frac{\partial\left(V_f^m C_f^{m'}\right)}{\partial z} = F_0\frac{k_p}{k_m}\frac{C_s^{m'}}{1-\phi_m} - F_0 S\frac{C_f^{m'}}{\phi_m} + \frac{F_0}{Da}\left(\frac{C_s^{m'}}{1-\phi_m} - k_m\frac{C_f^{m'}}{\phi_m}\right), \tag{A13}$$

$$\frac{\partial\left(C_s^{m'}\right)}{\partial t} + \frac{\partial\left(V_s^m C_s^{m'}\right)}{\partial z} = -F_0\frac{k_p}{k_m}\frac{C_s^{m'}}{1-\phi_m} - \frac{F_0}{Da}\left(\frac{C_s^{m'}}{1-\phi_m} - k_m\frac{C_f^{m'}}{\phi_m}\right), \tag{A14}$$

$$\phi_{ch} V_f^{ch} C_f^{ch} = \int_0^z dz\cdot F_0 S\frac{1-\psi}{\psi}\frac{C_f^{m'}}{\phi_m}. \tag{A15}$$

To minimize errors in numerical integrations of this advection-dominated problem, we use a fourth-order Runge-Kutta Discontinuous Galerkin method (Shu and Osher, 1988; Cockburn and Shu, 1989) to solve the time-

dependent Eqs. (A13) and (A14). We use the software package deall.ii (Bangerth et al., 2016) to implement the numerical scheme.

APPENDIX B. EMPIRICAL EXPRESSIONS FOR THE VARIATION OF ISOTOPE RATIOS

The systematic trend of the pooled melt as a function of the 2D enrichment strength shown in Fig. 6 can be used to estimate not only the average isotopic composition of the pooled melt but also the range of isotope ratios in the well-mixed pooled melt if the following three sets of parameters are known: (1) the composition and proportion of endmembers, (2) the 2D enrichment strength, and (3) the average spacing. The former determines the average of the pooled melt and the latter two determine the variability of the well-mixed pooled melt. The enriched and depleted bounds of the pooled melt (using a 100 km-wide melt pooling area) shown in Fig. 6 are given by the following two empirical expressions:

$$\text{“Enriched bound”} = \frac{X_{mean} + X_E \cdot f}{Y_{mean} + Y_E \cdot f}, \tag{B1}$$

$$\text{“Depleted bound”} = \frac{X_{mean} + X_E \cdot g}{Y_{mean} + Y_E \cdot g}, \tag{B2}$$

$$f = a \cdot L\sqrt{\omega}, \tag{B3}$$

$$g = \omega \cdot \left[\exp\left(-b \cdot \frac{1-\omega}{\omega} \cdot L\right) - 1\right], \tag{B4}$$

where X and Y are the concentration of the numerator and the denominator of the isotope ratio (X/Y), respectively; ω is the volume proportion of the enriched endmember in the mantle source; f (>0) and g (<0) are two short-hand notations; a and b are two element-specific parameters and their values (Table B1) depend on the melting Damköhler number and partition coefficient; subscripts “D” and “E” refer to the concentration in DMM and the enriched endmember, respectively; subscript “mean” indicates the mean concentration in the two-component source. As shown in Table B1, values of a and b for Pb and Sr are larger than those for Nd and Hf, which is consistent with the results that isotopic signals Nd and Hf are better mixed than those of Sr and Pb if the enrichment factor of all elements are the same.

By substituting the mean concentration in the right-hand side of Eqs. (B1) and (B2) into the two-component mixing equation (Langmuir et al., 1978), we can rewrite the “Enrichment bound” and the “Depleted bound” in terms of isotope ratios of the enriched and depleted endmember components:

Table B1
Parameters in the “enriched bound” and “depleted bound” for well-mixed pooled melt.

	Nd	Hf	Sr	Pb
a (km^{-1})	2.55×10^{-2}	2.30×10^{-2}	3.67×10^{-2}	4.62×10^{-2}
b (km^{-1})	9.34×10^{-3}	8.85×10^{-3}	1.29×10^{-2}	1.23×10^{-2}

$$\text{“Enriched bound”} = \frac{(1-\omega)\cdot\left(\frac{X}{Y}\right)_D + EMX\cdot(\omega+f)\cdot\left(\frac{X}{Y}\right)_E}{(1-\omega)+EMX\cdot(\omega+f)}, \tag{B5}$$

$$\text{“Depleted bound”} = \frac{(1-\omega)\cdot\left(\frac{X}{Y}\right)_D + EMX\cdot(\omega+g)\cdot\left(\frac{X}{Y}\right)_E}{(1-\omega)+EMX\cdot(\omega+g)}. \tag{B6}$$

It can be shown that $EMX \cdot f$ is a function of the 2D enrichment strength (Eq. (7)) and $EMX \cdot g$ is a function of the average spacing (Eq. (8)). $EMX \cdot \omega$ is effectively constant in the simulations presented in Fig. 6 because the average composition of the source is fixed. Results of Eqs. (B5) and (B6) are plotted as contours in Fig. 7 and Fig. S9 where the dependence of the “Enriched bound” and the “Depleted bound” on $EMX \cdot L^2$ and $EMX \cdot L$, respectively, are clearly demonstrated. Note that Eqs. (B1), (B2), (B5), and (B6) recover the two-component mixing equation (Langmuir et al., 1978) if f and g are zero. The positive valued f and the negative valued g represent the fluctuation due to specific size, spacing, and concentration of enriched heterogeneities.

The variation of isotope ratios in the pooled melt predicted by Eqs. (B5) and (B6) only applies to a 100 km-wide melt pooling area. For an arbitrary width of melt pooling area, we replace the size of the heterogeneity in Eqs. (B3) and (B4) with an equivalent size, L^*, according to the scaling relationship discussed in Section 4.4 (Fig. 9):

$$L^* = L \cdot \sqrt{\frac{w_{p100}}{w_p}}, \tag{B7}$$

where the reference width of melt pooling area w_{p100} is 100 km.

APPENDIX C. SUPPLEMENTARY MATERIAL

Supplementary figures and captions for supplementary movies can be found in “Electronic Supplementary Materials”. Supplementary data to this article can be found online at https://doi.org/10.1016/j.gca.2019.10.013.

REFERENCES

Asimow P. D., Dixon J. E. and Langmuir C. H. (2004) A hydrous melting and fractionation model for mid-ocean ridge basalts: Application to the Mid-Atlantic Ridge near the Azores. *Geochem. Geophys. Geosyst.* **5**(1). https://doi.org/10.1029/2003GC000568.

Asimow P. D. and Langmuir C. (2003) The importance of water to oceanic mantle melting regimes. *Nature* **421**(6925), 815–820.

Bangerth W., Davydov D., Heister T., Heltai L., Kanschat G., Kronbichler M., Maier M., Turcksin B. and Wells D. (2016) The deal.II Library, Version 8.4. *J. Numer. Math.* **24**, 135.

Bloch E. and Ganguly J. (2014) ^{176}Lu–^{176}Hf and ^{147}Sm–Nd ages of the Martian shergottites: Evaluation of the shock-resetting hypothesis through diffusion kinetic experiments and modeling, and petrological observations. *Earth Planet. Sci. Lett.* **395**, 173–183.

Bo T., Katz R. F., Shorttle O. and Rudge J. F. (2018) The melting column as a filter of mantle trace-element heterogeneity. *Geochem. Geophys. Geosyst.*, https://doi.org/10.1029/2018GC007880.

Cherniak D. J. (1998) Pb diffusion in clinopyroxene. *Chem. Geol.* **150**(1–2), 105–117.

Cockburn B. and Shu C.-W. (1989) TVB Runge-Kutta local projection discontinuous Galerkin finite element method for conservation laws. II. General framework. *Math. Comput.* **52** (186), 411–435.

Cordier C., Benoit M., Hémond C., Dyment J., Le Gall B., Briais A. and Kitazawa M. (2010) Time scales of melt extraction revealed by distribution of lava composition across a ridge axis. *Geochem. Geophys. Geosyst.* **11**(7).

Courtillot V., Davaille A., Besse J. and Stock J. (2003) Three distinct types of hotspots in the Earth's mantle. *Earth Planet. Sci. Lett.* **205**(3–4), 295–308.

DePaolo D. J. (1996) High-frequency isotopic variations in the Mauna Kea tholeiitic basalt sequence: Melt zone dispersivity and chromatography. *J. Geophys. Res. Solid Earth* **101**(B5), 11855–11864.

Ghods A. and Arkani-Hamed J. (2000) Melt migration beneath mid-ocean ridges. *Geophys. J. Inter.* **140**(3), 687–697.

Gurnis M. and Davies G. F. (1986) Mixing in numerical models of mantle convection incorporating plate kinematics. *J. Geophys. Res.: Solid Earth (1978–2012)* **91**(B6), 6375–6395.

Hebert L. B. and Montési L. G. J. (2010) Generation of permeability barriers during melt extraction at mid-ocean ridges. *Geochem. Geophys. Geosyst.* **11**(12).

Hofmann A. (2003) Sampling mantle heterogeneity through oceanic basalts: isotopes and trace elements. *Treatise Geochem.* **2**, 61–101.

Holness M. B. and Richter F. M. (1989) Possible effects of spreading rate on Morb isotopic and rare earth composition arising from melting of a heterogeneous source. *J. Geol.* **97**(3), 247–260.

Ito G. and Mahoney J. J. (2005a) Flow and melting of a heterogeneous mantle: 1. Method and importance to the geochemistry of ocean island and mid-ocean ridge basalts. *Earth Planet. Sci. Lett.* **230**(1–2), 29–46.

Ito G. and Mahoney J. J. (2005b) Flow and melting of a heterogeneous mantle: 2. Implications for a chemically nonlayered mantle. *Earth Planet. Sci. Lett.* **230**(1), 47–63.

Iwamori H. (1993) A model for disequilibrium mantle melting incorporating melt transport by porous and channel flows. *Nature* **366**(6457), 734–737.

Kelemen P. B., Braun M. and Hirth G. (2000) Spatial distribution of melt conduits in the mantle beneath oceanic spreading ridges: Observations from the Ingalls and Oman ophiolites. *Geochem. Geophys. Geosyst.* **1**(7).

Kelemen, P. B., Yogodzinski, G. M. and Scholl, D. W. (2003). Along-Strike Variation in the Aleutian Island Arc: Genesis of High Mg# Andesite and Implications for Continental Crust. Inside the subduction factory pp. 223–276.

Keller T., Katz R. F. and Hirschmann M. M. (2017) Volatiles beneath mid-ocean ridges: Deep melting, channelised transport, focusing, and metasomatism. *Earth Planet. Sci. Lett.* **464**, 55–68.

Kinzler R. J. and Grove T. L. (1992) Primary magmas of mid-ocean ridge basalts 2. Applications. *J. Geophys. Res. Solid Earth* **97**(B5), 6907–6926.

Langmuir C. H., Vocke, Jr, R. D., Hanson G. N. and Hart S. R. (1978) A general mixing equation with applications to Icelandic basalts. *Earth Planet. Sci. Lett.* **37**(3), 380–392.

Laubier M., Gale A. and Langmuir C. H. (2012) Melting and crustal processes at the FAMOUS segment (Mid-Atlantic Ridge): new insights from olivine-hosted melt inclusions from multiple samples. *J. Petrol.* **53**(4), 665–698.

Lehnert K., Su Y., Langmuir C. H., Sarbas B. and Nohl U. (2000) A global geochemical database structure for rocks. *Geochem. Geophys. Geosyst.* **1**(5), https://doi.org/10.1029/1999GC000026.

Liang Y. (2003) On the thermo-kinetic consequences of slab melting. *Geophys. Res. Lett.* **30**(24), 2270.

Liang Y. (2008) Simple models for dynamic melting in an upwelling heterogeneous mantle column: Analytical solutions. *Geochim. Cosmochim. Acta* **72**(15), 3804–3821.

Liang Y. and Peng Q. (2010) Non-modal melting in an upwelling mantle column: Steady-state models with applications to REE depletion in abyssal peridotites and the dynamics of melt migration in the mantle. *Geochim. Cosmochim. Acta* **74**(1), 321–339.

Liang Y. and Liu B. (2016) Simple models for disequilibrium fractional melting and batch melting with application to REE fractionation in abyssal peridotites. *Geochim. Cosmochim. Acta* **173**, 181–197.

Liang Y. and Liu B. (2018) Stretching chemical heterogeneities by melt migration in an upwelling mantle: An analysis based on time-dependent batch and fractional melting models. *Earth Planet. Sci. Lett.* **498**, 275–287.

Liang Y., Schiemenz A., Hesse M. A. and Parmentier E. M. (2011) Waves, channels, and the preservation of chemical heterogeneities during melt migration in the mantle. *Geophys. Res. Lett.* **38**(20).

Liu B. (2018) *Melt migration dynamics and trace element fractionation beneath mid-ocean ridges*. Brown University.

Liu C.-Z., Snow J. E., Hellebrand E., Brugmann G., von der Handt A., Buchl A. and Hofmann A. W. (2008) Ancient, highly heterogeneous mantle beneath Gakkel ridge, Arctic Ocean. *Nature* **452**(7185), 311–316.

Liu B. and Liang Y. (2017a) The prevalence of kilometer-scale heterogeneity in the source region of MORB upper mantle. *Sci. Adv.* **3**(11).

Liu B. and Liang Y. (2017b) An introduction of Markov chain Monte Carlo method to geochemical inverse problems: Reading melting parameters from REE abundances in abyssal peridotites. *Geochim. Cosmochim. Acta* **203**, 216–234.

Liu B. and Liang Y. (2019) The importance of permeability and deep channel network on the distribution of melt, fractionation of REE in abyssal peridotites, and U-series disequilibria in basalts beneath mid-ocean ridges: A numerical study using a 2D double-porosity model. *Earth Planet. Sci. Lett.* **528**, 115788.

Lundstrom C. (2000) Models of U-series disequilibria generation in MORB: the effects of two scales of melt porosity. *Phys. Earth Planet. Inter.* **121**(3–4), 189–204.

McDonough W. F. and Sun S. S. (1995) The composition of the Earth. *Chem. Geol.* **120**(3–4), 223–253.

Morgan J. P. (1987) Melt migration beneath mid-ocean spreading centers. *Geophys. Res. Lett.* **14**(12), 1238–1241.

Morgan J. P. and Morgan W. J. (1999) Two-stage melting and the geochemical evolution of the mantle: a recipe for mantle plum-pudding. *Earth Planet. Sci. Lett.* **170**(3), 215–239.

Navon O. and Stolper E. (1987) Geochemical Consequences of Melt Percolation: The Upper Mantle as a Chromatographic Column. *J. Geol.* **95**(3), 285–307.

O'Hara M. J. (1985) Importance of the 'shape' of the melting regime during partial melting of the mantle. *Nature* **314**(6006), 58–62.

Plank T. and Langmuir C. H. (1992) Effects of the melting regime on the composition of the oceanic crust. *J. Geophys. Res. Solid Earth* **97**(B13), 19749–19770.

Plank T., Spiegelman M., Langmuir C. H. and Forsyth D. W. (1995) The meaning of "mean F": Clarifying the mean extent of melting at ocean ridges. *J. Geophys. Res. Solid Earth* **100**(B8), 15045–15052.

Rudge J. F., Maclennan J. and Stracke A. (2013) The geochemical consequences of mixing melts from a heterogeneous mantle. *Geochim. Cosmochim. Acta* **114**, 112–143.

Saal A. E., Hart S. R., Shimizu N., Hauri E. H. and Layne G. D. (1998) Pb Isotopic Variability in Melt Inclusions from Oceanic Island Basalts, Polynesia. *Science* **282**(5393), 1481–1484.

Sanfilippo A., Salters V., Tribuzio R. and Zanetti A. (2019) Role of ancient, ultra-depleted mantle in Mid-Ocean-Ridge magmatism. *Earth Planet. Sci. Lett.* **511**, 89–98.

Schiemenz, A., Hesse, M., Hesthaven, J., Liang, Y., & Parmentier, E. M. (2008). A Possible Link between Mantle Heterogeneity and Dunite Channel Distribution in an Upwelling Mantle: A Numerical Study. AGU Fall Meeting Abstracts.

Shu C.-W. and Osher S. (1988) Efficient implementation of essentially non-oscillatory shock-capturing schemes. *J. Comput. Phys.* **77**(2), 439–471.

Sinton J. M. and Detrick R. S. (1992) Mid-ocean ridge magma chambers. *J. Geophys. Res. Solid Earth* **97**(B1), 197–216.

Slater L., Mckenzie D., Grönvold K. and Shimizu N. (2001) Melt generation and movement beneath Theistareykir, NE Iceland. *J. Petrol.* **42**(2), 321–354.

Sneeringer M., Hart S. R. and Shimizu N. (1984) Strontium and samarium diffusion in diopside. *Geochim. Cosmochim. Acta* **48**(8), 1589–1608.

Sparks D. W. and Parmentier E. M. (1991) Melt extraction from the mantle beneath spreading centers. *Earth Planet. Sci. Lett.* **105**(4), 368–377.

Spiegelman M. (1993) Physics of Melt Extraction: Theory, Implications and Applications. *Philos. Trans.: Phys. Sci. Eng.* **342**(1663), 23–41.

Spiegelman M. and Kelemen P. B. (2003) Extreme chemical variability as a consequence of channelized melt transport. *Geochem. Geophys. Geosyst.* **4**(7).

Spiegelman M. and McKenzie D. (1987) Simple 2-D models for melt extraction at mid-ocean ridges and island arcs. *Earth Planet. Sci. Lett.* **83**(1), 137–152.

Stracke A. (2012) Earth's heterogeneous mantle: A product of convection-driven interaction between crust and mantle. *Chem. Geol.* **330–331**, 274–299.

Stracke A., Bizimis M. and Salters V. J. M. (2003) Recycling oceanic crust: Quantitative constraints. *Geochem. Geophys. Geosyst.* **4**(3), https://doi.org/10.1029/2001GC000223.

Stracke A., Bourdon B. and McKenzie D. (2006) Melt extraction in the Earth's mantle: Constraints from U–Th–Pa–Ra studies in oceanic basalts. *Earth Planet. Sci. Lett.* **244**(1), 97–112.

Stracke A. and Bourdon B. (2009) The importance of melt extraction for tracing mantle heterogeneity. *Geochim. Cosmochim. Acta* **73**(1), 218–238.

Sun C. and Liang Y. (2012) Distribution of REE between clinopyroxene and basaltic melt along a mantle adiabat: effects of major element composition, water, and temperature. *Contrib. Mineral. Petrol.* **163**(5), 807–823.

Van Orman J. A., Grove T. L. and Shimizu N. (2001) Rare earth element diffusion in diopside: influence of temperature, pressure, and ionic radius, and an elastic model for diffusion in silicates. *Contrib. Miner. Petrol.* **141**(6), 687–703.

Wanless V. D., Behn M. D., Shaw A. M. and Plank T. (2014) Variations in melting dynamics and mantle compositions along the Eastern Volcanic Zone of the Gakkel Ridge: insights from olivine-hosted melt inclusions. *Contrib. Miner. Petrol.* **167**(5), 1005.

Weatherley S. M. and Katz R. F. (2016) Melt transport rates in heterogeneous mantle beneath mid-ocean ridges. *Geochim. Cosmochim. Acta* **172**, 39–54.

White W. M. and Klein E. M. (2014) *4.13 - Composition of the Oceanic Crust*, second ed. Elsevier, Oxford, pp. 457–496.

Workman R. K. and Hart S. R. (2005) Major and trace element composition of the depleted MORB mantle (DMM). *Earth Planet. Sci. Lett.* **231**(1–2), 53–72.

Yao, L., Dygert, N., Peterson, M., Sun, C., Wetzel, D. and Liang, Y. (2010). "A bundle of columns" model for trace element fractionation during melting and melt migration in a vertically upwelling, chemically and lithologically heterogeneous mantle. AGU Fall Meeting Abstracts.

Yao L., Sun C. and Liang Y. (2012) A parameterized model for REE distribution between low-Ca pyroxene and basaltic melts with applications to REE partitioning in low-Ca pyroxene along a mantle adiabat and during pyroxenite-derived melt and peridotite interaction. *Contrib. Mineral. Petrol.* **164**(2), 261–280.

Zindler A. and Hart S. (1986) Chemical Geodynamics. *Annu. Rev. Earth Planet. Sci.* **14**, 493–571.

Associate editor: Janne Blichert-Toft